Design, Fabrication, and Modification of Cost-Effective Nanostructured TiO_2 for Solar Energy Applications

Meidan Ye, Miaoqiang Lv, Chang Chen, James Iocozzia, Changjian Lin and Zhiqun Lin

Abstract One of the greatest challenges for human society and civilization is the development of powerful technologies to harness renewable solar energy to satisfy the ever-growing energy demands. Semiconductor nanomaterials have important applications in the field of solar energy conversion. Among these, TiO_2 represents one of the most promising functional semiconductors and is extensively utilized in photoelectrochemical applications, including photocatalysis (e.g., H_2 generation from water splitting) and photovoltaics (e.g., dye-sensitized solar cells, DSSCs). As such, many efforts have focused on developing and exploiting cost-effective nanostructured TiO_2 materials for efficient solar energy applications.

1 Introduction

With worldwide economic development and population growth, global energy demands have increased dramatically. Today, such demands largely depend on nonrenewable oil and fossil fuels. The continuous rise in the price of oil and gas has motivated people to pay closer attention to issues concerning our energy supply and demand [1]. In the twentieth century alone, the world population quadrupled and energy demand went up 16 times. The exponential energy demand is exhausting fossil fuel supplies at an alarming rate. The mean global energy

M. Ye · M. Lv · C. Chen · C. Lin (✉)
State Key Laboratory of Physical Chemistry of Solid Surfaces,
Department of Chemistry, College of Chemistry and Chemical Engineering,
Xiamen University, Xiamen 361005, China
e-mail: cjlin@xmu.edu.cn

J. Iocozzia · Z. Lin (✉)
School of Materials Science and Engineering, Georgia Institute of Technology,
Atlanta, GA 30332, USA
e-mail: zhiqun.lin@mse.gatech.edu

Z. Lin and J. Wang (eds.), *Low-cost Nanomaterials*, Green Energy and Technology,
DOI: 10.1007/978-1-4471-6473-9_2,

consumption rate was 4.1×10^{20} J, or 13 terawatts (TW) in 2000. By year 2050, the number will have doubled to 28 TW and tripled to 46 TW by the end of the century based on current estimates of population growth and energy consumption [2]. Currently, this huge energy demand is supplied by oil (35 %), coal (23 %) and natural gas (21 %), which in total yields a ratio of around 79 % from fossil fuels. While biomass provides only 8 % of the energy supply, nuclear energy only 6.5 %, and hydropower a mere 2 % share [1]. Excessive extraction is leading to gradually decreasing reserves of conventional, nonrenewable, energy resources, such as oil, coal, and natural gas. Moreover, the increasing energy production concurrently impacts the environment through the production of greenhouse gases (i.e., carbon dioxide, methane, nitrous oxide, and other gases) from fossil fuels, which contribute to climate change and even global warming concerns [3]. Therefore, in order to deal with the increasing energy demand and provide a long-term solution to the energy crisis in the future it is essential to develop environmentally and economically clean alternative energy resources in order to achieve a globally sustainable society.

Renewable energy resources, including hydroelectricity from tides and ocean currents (2.5 TW), geothermal energy (12 TW), wind power (24 TW), and solar energy striking the earth (170,000 TW) are considered highly promising options [3]. Among these, solar energy is clean, endlessly abundant, and has the largest potential to satisfy the future global demand for renewable energy sources (under ideal conditions, radiation power on a horizontal surface is 1000 Wm^{-2}) [2]. However, to date, the energy converted from sunlight remains far less than that of the total energy demand. For instance, the total average annual installed energy capacity in 2009 was about 7 gigawatts (GW), which only contributed to 0.2 % of global electricity usage [4]. Thus, the efficient, direct conversion of solar energy into electricity and fuels should, and must, be one of the most important scientific and technological pursuits of this century [5].

1.1 Applications for Solar Cells

First of all, to become a major contributor to future renewable energy, solar energy must be cost-effective and priced competitively relative to conventional energy resources, nuclear power, and other renewable energy resources [6]. Currently, the direct conversion of incident solar photons to electricity is achieved through photovoltaic (PV) devices (or solar cells) [7, 8]. Single crystal silicon-based PV devices are the first-generation solar cells, which are commercially available for installation, deliver power with a 15 % efficiency and make up about 90 % of the current PV market. However, first-generation solar cells still suffer from several inherent deficiencies as a result of the complicated and energy intensive fabrication process, inevitable use of toxic chemicals, heavy cell weight, and the high cost of manufacturing and installation [9]. A retail price of about $2 per peak watt (Wp) with a corresponding production price of about $0.5/Wp could make PV cost-competitive

with electricity produced from coal. But the production cost of these first-generation solar cells is presently around $3.5/Wp, which is highly dependent on the price of the silicon material [10].

Second-generation solar cells, including amorphous (or nano-, micro-, poly-) silicon, $CuInGaSe_2$ (CIGS), and CdTe, are based on thin film technologies. These thin film solar cells possess some advantages, such as relatively simple manufacturing processes which reduce the production cost to about $1/Wp, multiple choices of applied materials, and the possibility of flexible substrates. However, second-generation solar cells face several shortcomings as well such as the toxicity (e.g., Cd) and low abundance (e.g., In and Se) of the component materials. Moreover, it is necessary to further increase their efficiency for practical utilization [11]. Both the first- and second-generation solar cells are based on single junction devices which must obey the Shockley-Queisser limit with a maximum thermodynamic efficiency of 31–33 % when the optimum band gaps fall between about 1.1 and 1.4 eV [12].

Significantly, the third-generation solar cells, including tandem cells, hot carrier cells, dye-sensitized solar cells, and organic solar cells can overcome this thermodynamic efficiency limit. The most important thing is that these third-generation solar cells are promising to convert solar energy into electricity at a highly competitive price, that is, less than $0.5/Wp [2, 10].

Among these third-generation solar cells, DSSCs offer many attractive features that facilitate market entry. They afford low production cost (i.e., inexpensive to manufacture, possibility of roll-to-roll processing and low embodied energy), low-toxicity, earth-abundant materials (except Pt and Ru), good performance in diverse light conditions (i.e., high angle of incidence, low intensity and partial shadowing), lightweight, flexible, and design feasibility (i.e., transparent, bifacial and selected colors) [2, 13]. Since the first DSSC was reported with efficiency of 7.1 % in 1991 [14], much attention has been devoted to this promising electrochemical device. After two decades of concentrated efforts, DSSCs have developed into a powerful photovoltaic technology with a recorded efficiency as high as 12.3 % [15].

Typically, a DSSC is made of five components: a conductive mechanical support (e.g., transparent conductive glass or Ti foil), a semiconductor film (e.g., TiO_2), a sensitizer (e.g., ruthenium dye N719), an electrolyte (e.g., iodide/triiodide couple), and a counter electrode (e.g., Pt-coated electrode). The operating principles of DSSCs are further described in Fig. 1a [16]. In DSSCs, electricity is created at the semiconductor film on which a monolayer of visible light absorbing dye is chemisorbed. Photo-excitation of the absorbed dye molecules generates excited electrons which are further injected into the conduction band of the semiconductor and quickly migrated to the external circuit through the conductive substrate. The original state of the dye is subsequently restored by electron donation from the electrolyte, usually an organic solvent containing a redox system, such as the iodide/triiodide (I^-/I_3^-) couple. The regeneration of the sensitizer by I^- prevents the recapture of the conduction band electron by the oxidized dye while I^- is regenerated in turn by the reduction of I_3^- at the counter electrode. The counter electrode returns charge from the external circuit back to the cycling

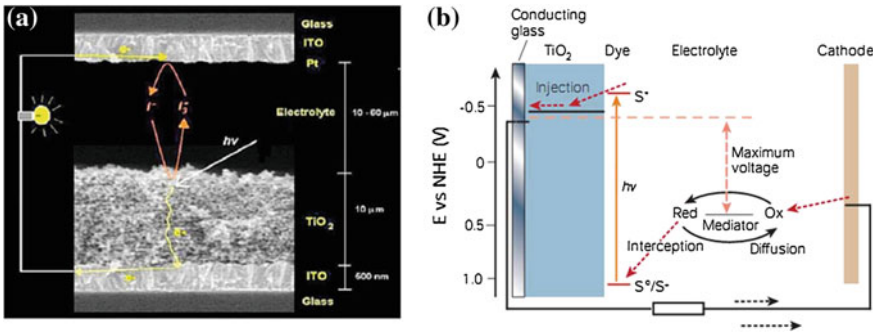

Fig. 1 **a** The physical image and **b** the simple operating principle of DSSCs based on TiO_2 nanomaterials. (Reprinted with permission from Ref. **a** [17], **b** [9]. Copyright © Wiley-VCH and Nature Publishing Group)

circuit in the cell [17]. The voltage generated under illumination depends on the difference between the Fermi level of the electron in the semiconductor materials and the redox potential of the electrolyte (Fig. 1b) [18, 19].

Notably, the core of the system is the nanoporous semiconductor, composed primarily of TiO_2 materials, which not only supplies numerous adsorption sites for dye sensitizer but also functions as an electron acceptor and electronic conductor [16]. TiO_2 possesses several unique chemical and physical properties which make it the most popular candidate for semiconductors in DSSCs. First, the conduction band edge of TiO_2 lies slightly below the excited state energy level of many sensitized dyes, which is a necessary condition for efficient electron injection. Second, TiO_2 also has a large dielectric constant ($\varepsilon = 80$ for anatase) for effective electrostatic shielding of the injected electrons from the oxidized dye molecules adsorbed on the TiO_2 surface, thus avoiding their recombination before regeneration of the dyes by the redox electrolyte. The relatively high refractive index of TiO_2 (n = 2.5 for anatase) also provides efficient diffusive light scattering inside the nanoporous film, thus significantly increasing the light harvesting potential. In addition, TiO_2 is stable over a wide range of environments, such as high temperature and high acidity. Lastly, TiO_2 is inexpensive, abundant, and nontoxic [2, 20]. In order to improve upon the aforementioned useful properties, over the past several decades extensive research interests and efforts have focused on the design, fabrication, and modification of versatile TiO_2 photoanodes.

1.2 Applications in Photoelectrochemical Water Splitting

In addition, another ideal way for direct conversion of solar energy into practical energy sources is through the generating of hydrogen from solar photoelectrochemical splitting of water using semiconductors as photoelectrodes [21].

Hydrogen is a well-known, potentially highly efficient and environmentally clean fuel since the chemical energy stored in the H–H bond can be easily released when the molecule reacts with oxygen to yield only water as a by-product (i.e., combustion). Moreover, hydrogen is a light gas (0.08988 g/L) with a higher energy density compared to any other fuel such as gasoline. For example, one gram of hydrogen can provide about 140 kJ of energy, which is almost four times that of methane (33 kJ/g) [22]. Therefore, large-scale and cost-effective generation of hydrogen, preferably using renewable and carbon-free resources, is highly attractive. Currently, hydrogen is produced from a variety of primary sources such as natural gas, heavy oil, methanol, biomass, wastes, coal, solar, wind, and nuclear power. Among these sources, hydrogen production from photocatalytic water splitting in the presence of semiconductor photocatalysts using solar irradiation represents one of the most promising approaches and has garnered attention because of its direct use of sunlight. In so doing, the process avoids the inefficiencies due to thermal transformation or electrolysis with the conversion of solar energy to electricity [23]. Since the pioneering work by Fujishima and Honda in 1972 on a photoelectrochemical cell (PEC) using a TiO_2 photoelectrode, water splitting under sunlight has made remarkable progress in the past 40 years [24, 25].

Water splitting is a thermodynamically uphill or endothermic process with a significantly positive change in Gibbs free energy ($\Delta G^o = +237.2$ kJ/mol, 1.23 eV per electron), and a minimum potential of 1.23 eV is needed for the reaction to proceed. Taking the recombination of excited electron-hole pairs and losses from devices such as contacts and electrode resistances into consideration, the optimal energy required for water splitting is around 2 eV [22]. In a PEC, the key components are the electrodes (i.e., cathode and anode) on which redox chemical reactions involving electron transfer take place. Typically, a PEC cell is composed of a semiconductor photoanode and a Pt counter electrode in an electrolyte solution. As shown in Fig. 2a, incident light irradiation with the photon energy matching or greater than the forbidden band gap energy (E_g) of the semiconductor generates electron-hole pairs and the photo-excited electrons are then promoted from the valence band (VB) to the unoccupied conduction band (CB), which then migrate to the cathode and react with protons to generate hydrogen ($2H^+ + 2e^- \rightarrow H_2$). Concurrently, the holes accumulate on the surface of the photoanode and split water molecules to produce oxygen ($H_2O + 2h^+ \rightarrow 2H^+ + 1/2O_2$) [26].

To effectively split water for hydrogen generation, the match of the band gap and the potential of the conduction and valence bands are important, that is, the E_g of the semiconductor should be larger than 1.23 eV ($\lambda < 1000$ nm) to realize water splitting. However, when using visible light, E_g should be less than 3.0 eV ($\lambda > 400$ nm) [27]. In addition, the semiconductor photoanode with a conduction band edge more negative than the H_2 evolution potential and a valence band edge more positive than the O_2 evolution potential is also required. Other requirements include stability under light irradiation and in aqueous solution, excellent absorption in the solar spectrum region, high-quality structure for effective charge transport, and low production cost [28]. Unfortunately, no such material has been found that can satisfy all the requirements simultaneously.

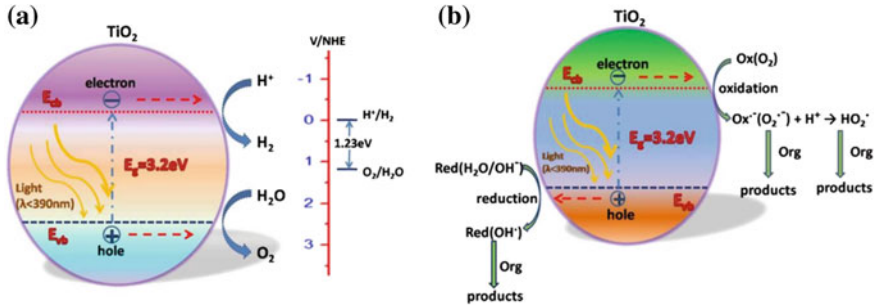

Fig. 2 **a** Overview principle of TiO_2-based photocatalytic water splitting for hydrogen generation. **b** Simplified principle of TiO_2-based photocatalysis of organic pollutants. (Reprinted with permission from Ref. [29]. Copyright © Simplex Academic Publishers)

Numerous semiconductor materials, for instance (TiO_2, Fe_2O_3, $SrTiO_3$, ZrO_2, WO_3, CdS, ZnO, $NaTaO_3$, $BaTi_4O_9$, $BiVO_4$, CeO_2) have been explored for water splitting into H_2 and O_2 under ultraviolet (UV) or visible light irradiation [23, 28, 29]. Among the various candidates for the photoanode, TiO_2 is considered to be one of the most promising semiconductor materials as it can fulfill the task of photocatalytic water splitting in a clean, environmentally friendly and low-cost way, owing to its favorable band gap energy (3.2 eV in anatase), high photochemical stability, non-toxic property, and relatively inexpensive cost [25]. There are however several drawbacks to TiO_2. The conversion efficiency of this technology is still low and thus it is currently only in the research stage. Also, the band gap of anatase TiO_2 is around 3.2 eV, implying that only ultraviolet (UV) light can be used for water splitting. Lastly, the PEC cell concurrently undergoes a rapid recombination of photogenerated electron-hole pairs [30]. Consequently, many research efforts are made to reduce these drawbacks in the TiO_2-based PEC cell.

1.3 Applications in Photocatalytic Degradation of Pollutants

Lastly, solar light may have the potential to solve the environmental contamination problem. Wastewater pollutants have become a worldwide environmental threat as a result of burgeoning industry and population [31]. To date, many techniques have been developed for the decontamination of many artificial or anthropogenic organic pollutants, especially those with high toxicity but very low concentration. A better alternative should be able to chemically transform the organic pollutants into environmentally benign compounds in an efficient manner [31].

Recently, numerous studies have been performed on the application of photocatalysis in the degradation of organic pollutants from wastewaters due to its ability to completely mineralize the toxic organic chemicals into nontoxic inorganic minerals [29]. Photocatalysis is triggered by semiconductor catalysts which

function as sensitizers for light-induced redox-reactions and have the unique electronic structure of a filled valence band, and an empty conduction band. On irradiation (Fig. 2b), electrons in the valence band of semiconductors are excited to their conduction band, thus leaving holes behind. The resulting electron-hole pairs can recombine or react separately with other molecules. The holes may migrate to the surface and react either with electron donors in the solution or with hydroxide ions to produce powerful oxidizing species like hydroxyl or superoxide radicals. Meanwhile, the conduction band electrons can reduce an electron acceptor [32]. Consequently, semiconductor materials can act as either an electron donor or as an electron acceptor for molecules in the surrounding medium, depending on the charge transfer to the adsorbed species [32].

Semiconductor nanomaterials are promising options for inexpensive and environmentally friendly decontamination systems in which the correlated chemical reagents, energy source, and catalysts are abundant, inexpensive, nontoxic, and produce no secondary pollution byproducts [33]. Compared to other semiconductors (e.g., ZnO, Fe_2O_3, CdS, and ZnS), TiO_2 is the most widely used semiconductor catalyst in photocatalysis due to its chemical and biological inertness, photostability, relative ease of manufacture and utilization, reaction catalysis efficiency, low cost, and nontoxicity. It does however have the disadvantage of solely ultraviolet (UV) activation and not visible [32].

2 Fabrication of Cost-Effective Nanostructured TiO_2 Materials

As mentioned above, TiO_2 is one of the most promising photovoltaic materials because of its appropriate electronic band structure, photostability, chemical inertness, and commercial availability [34]. TiO_2 exists in nature in three different polymorphs, namely, rutile, anatase, and brookite. In addition, other synthetic phases, for example, TiO_2(B), TiO_2(H), and TiO_2(R) as well as several high-pressure polymorphs have also been reported. Each phase shows different physical and chemical properties for different functionalities [34].

Of these phases, rutile and anatase are the most practically important crystal structures for energy applications (Table 1). In general, both anatase and rutile-type TiO_2 have a tetragonal crystal structure. The difference is that anatase TiO_2 follows a bipyramidal habit, while rutile TiO_2 obeys a prismatic habit [33]. These two tetragonal structures can be constructed by the chains of TiO_6 octahedra, where each Ti^{4+} ion is close to six O^{2-} ions. Anatase and rutile crystal structures are different in the distortion of each octahedron along with the assembly pattern of the octahedron chains. Specifically, the octahedron in rutile exhibits a slight orthorhombic distortion, while the octahedron in anatase is largely distorted, leading to lower symmetry compared to that of orthorhombic. Also, anatase has larger Ti–Ti distances but shorter Ti–O distances than those in rutile. Finally, the

Table 1 Physical and structural properties of anatase and rutile TiO_2. (Reprinted with permission from Ref. [33]. Copyright © Elsevier)

Property	Anatase	Rutile
Molecular weight (g/mol)	79.88	79.88
Melting point (°C)	1,825	1,825
Boiling point (°C)	2,500–3,000	2,500–3,000
Light absorption (nm)	<387.5	<413.3
Band-gap energy (eV)	~3.2	~3.0
Mohr's hardness	5.5	6.5–7.0
Dielectric constant	31	114
Density (g/cm^3)	3.79	4.13
Crystal structure	Tetragonal	Tetragonal
Space group	$I4_1/amd$	$P4_2/mnm$
Lattice constant (Å)	a = 3.78	a = 4.59
	c = 9.52	c = 2.96
Ti-0 bond length (Å)	1.94 (4)	1.95 (4)
	1.97 (2)	1.98 (2)

rutile structure is assembled by joining each octahedron with ten neighboring octahedrons in the form of two sharing edge oxygen pairs and eight sharing corner oxygen atoms. While for the anatase structure, each octahedron couples to eight neighbors with four sharing an edge and four sharing a corner. Thus, these differences in lattice structures result in different electronic properties between rutile and anatase TiO_2 [35]. Generally, anatase is considered to be more photoactive than rutile, largely due to the differences in the extent and nature of the surface hydroxyl groups present in the low temperature structure and the Fermi levels, where anatase ($E_g = 3.2$ eV) is about 0.2 eV higher than that of rutile ($E_g = 3.02$ eV). However, rutile TiO_2 still has some advantages over anatase such as higher chemical stability, higher refractive index, and cheaper production costs. Furthermore, rutile films have recently been used in DSSCs and have shown comparable performance to anatase DSSCs [36].

It is well accepted that the performance of devices is highly dependent on the chemical and physical properties of their as-prepared material components. Thus, today the demand for efficient, high performance devices has stimulated increasing attention in advanced functional materials [3]. Conventional micrometer-sized bulk materials suffer from inherent limitations in performance and fail to satisfy the increasing requirements of new devices. Consequently, nanostructured materials are becoming ever more important in many fields and hence have attracted great interest in recent years [34].

In brief, nanostructured materials exhibit quantum confinement effects when the electronic particles of these materials are confined by potential barriers to very small regions of space. The confinement can be in one dimension (i.e., quantum wells), in two dimensions (i.e., quantum wires, tubes or rods), or in three dimensions (i.e., quantum dots (QDs)). A variety of nanometer size-dependent properties have been found in the materials used in electrochemical energy

conversion and storage devices. For example, the increasing surface-to-volume ratio and special surface area facilitate sufficient reaction or interaction between the nanostructured material and surrounding electrolyte [37]. Energy conversion and transport in nanostructured materials are also different from those in bulk materials due to the quantum size effects on energy carriers such as photons, electrons, and molecules [38]. For example, efficient light harvesting to create charge carriers in materials happens at the scale of several hundreds of nanometers, near the wavelength of light.

However, the mean free path of the excited charge carriers is shorter than the wavelength of light, requiring the small length scales afforded by nanostructures. Considering the need for both efficient photon absorption and effective collection of excited charge carriers in devices, it is necessary to design structures on a scale commensurate with both the wavelength of light and charge migration lengths simultaneously. One such option is one-dimensional (1D) nanostructures (e.g., nanotubes or nanowires), which have one dimension larger than the wavelength of light, and another dimension shorter than the mean free path of charge carriers [39]. Accordingly, current efforts in nanoscience and nanotechnology for energy applications are concentrating on utilizing these nanoscale effects to produce efficient energy technologies such as solar cells, fuel cells, and batteries. Researchers are eager to exploit cost-effective process to prepare high-performance nanostructures for a more sustainable energy economy [6, 40–44].

Many properties of nanostructured TiO_2 films, such as surface area, shape, grain size, and grain boundary density, will significantly impact the performances of energy conversion devices [45–47]. The methodology used to fabricate the nanostructured films is an essential factor to tailor the properties of TiO_2 nanostructures [48]. To date, significant progress has been achieved in the preparation of TiO_2 nanomaterials. A variety of film preparation techniques have been developed and employed for the formation of diversiform nanostructured TiO_2, including nanoparticles [49], nanorods [50], nanowires [51], nanotubes [52], nanosheets [53], and mesoporous structures [54]. In most cases, nanostructured TiO_2 materials can be prepared either by dry or wet processes. In the past decades, a number of methods, such as sol–gel [55], hydrothermal/solvothermal processes [56], electrochemical anodization [57], electrospinning [58], electrospray [59], electrodeposition [60], directional chemical oxidation [61], ultrasound and microwave irradiation [62], laser pyrolysis [63], and chemical/physical vapor deposition [64], have been developed to control the size, morphology, and uniformity of TiO_2 nanostructures simultaneously. The following sections further elaborate on some of the above-mentioned preparation methods for preparing cost-effective, high-performance TiO_2 nanostructures for energy applications, such as DSSCs, hydrogen generation, and photocatalysis.

2.1 Preparation Methods

2.1.1 Sol–Gel Method

The sol–gel method is a powerful technique in the development of nanostructured semiconductor films with diverse morphologies. Sol–gel method is typically a two-step process of synthesis and deposition, and can easily tailor the material properties during synthesis under optimized conditions [65, 66]. In a typical sol–gel process, a colloidal suspension or sol is first obtained from the hydrolysis and polymerization reactions of the precursors, which are usually inorganic metal salts or metal organic compounds such as metal alkoxides. The phase conversion from the liquid sol into the solid gel phase is realized by complete polymerization and evaporation of the solvent. Finally, thin films of the resulting solid gel can be achieved via a variety of deposition techniques such as spin-coating, dip-coating, spray pyrolysis, doctor blade, electrophoretic, and template assisted deposition onto a conducting glass substrate (e.g., fluorine-doped tin oxide, FTO or indium-tin oxide, ITO glasses) or other preferred surface [67–69]. The film is then annealed at 200–450 °C in air for 1–2 h, which is essential to reduce grain boundaries and enhance crystallinity, thus improving electrical conductivity.

Nanostructured TiO_2 materials are usually prepared from the hydrolysis of a titanium precursor, which is normally performed via an acid-catalyzed hydrolysis step of titanium (IV) alkoxide (e.g., titanium isopropoxide, TTIP) or halide precursor (e.g., $TiCl_4$) followed by condensation. Properties of the resulting TiO_2 nanomaterials, including the crystallinity, morphology, structure size, surface area, porosity, degree of dispersion, and crystal phase, heavily depend on the reaction conditions, including the temperature, reaction time, solvent, solution pH, type of precursor, drying conditions, and post-treatment [20, 35, 70]. Among various methods, the sol–gel method is one of the most widely used methods for TiO_2 nanostructure preparation, due to its relatively low cost, flexibility of substrate, and diversity of nanostructures such as nanoparticles, nanorods, nanoporous films, and nanowires [1].

Template-assisted sol–gel processes are a well-established strategy for the design of various functional TiO_2 nanostructures. This method utilizes the morphological properties of known and characterized templates in order to assemble materials with a particular morphology by reactive deposition or dissolution methods. By controlling the morphology of the template material, it is possible to prepare numerous new materials with a regular and controllable morphology (e.g., mesoporous structure) on the nano and micro scale [71, 72]. The template-assisted method can be generally divided into three sequential steps as shown in Fig. 3a: (1) assembly of a template (e.g., composed of polymer latex spheres), (2) infiltration and deposition of TiO_2 nanoparticles or titanium precursor, and (3) selective removal of the used template to yield an inverse porous structure [73]. The used templates can be soft templates (surfactants or block polymers) or hard templates (porous silica, polystyrene spheres, or porous carbon) [74].

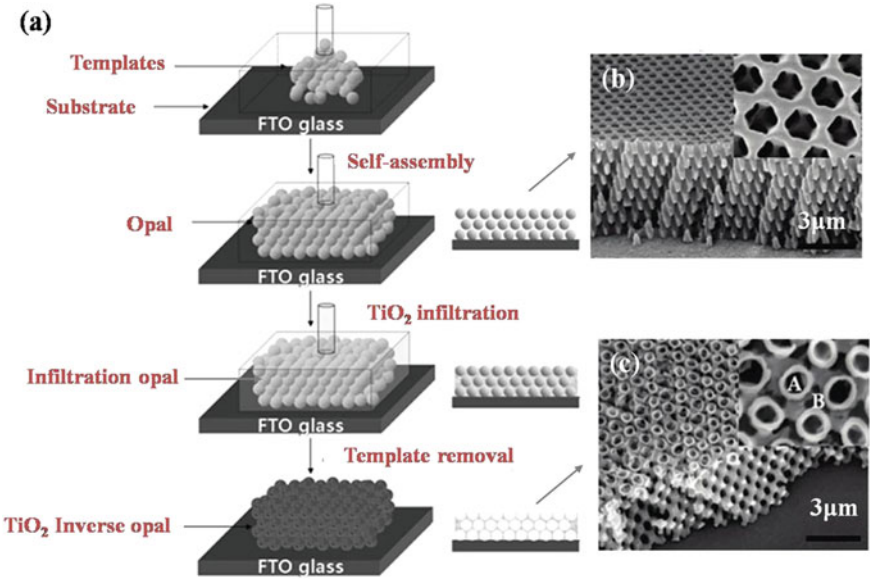

Fig. 3 **a** Schematics of the sol-gel fabrication procedure of a TiO_2 inverse opal via a template-assisted method. SEM images of SU8 templates (**b**) and TiO_2 inverse opal (**c**). (Reprinted with permission from Ref. **a** [92], **b**, **c** [72]. Copyright © Wiley-VCH and American Chemical Society)

In the past decade, mesoporous TiO_2 materials have attracted considerable interest for many applications due to their continuous particle framework, which contain nanoparticles distributed throughout structures of adjustable pore size and high specific surface area. Mesoporous TiO_2 materials with tailored pore size, high specific surface area, and well-defined crystalline structure in particular have potential applications in solar cells, photocatalysis, and water splitting [75, 76]. In photocatalytic applications, a tunable pore size can facilitate the diffusion rate of reactants toward adsorption sites, while a high surface area can maximize the interface between the reactant and the catalyst surfaces [77]. For DSSCs, mesoporous TiO_2 can enhance light harvesting within the electrodes without sacrificing the accessible surface for dye loading [78].

Generally, the sol–gel process using organic surfactants as assisting templates represents the most widely used route for the synthesis of mesoporous TiO_2 and involves a complicated mechanism called evaporation-induced self-assembly (EISA) [79]. The EISA process produces an ideal grid-like morphology consisting of a continuous, ordered network of anatase TiO_2 with a high surface area by condensation of a titanium precursor around self-organized organic templates in a gel phase, followed by removal of the templates via heat treatment. This simple process uses a wide range of surfactants as structure directing agents to prepare ordered mesoporous TiO_2. The structure directing agent in this method is an amphiphilic macromolecule (block copolymer) which microphase-separates into

ordered domains on the 5–50 nm length scale. This is driven by the incompatibility of its covalently linked macro-molecular blocks. The inorganic material is typically selectively incorporated into one of the polymer domains in the form of a nanoparticle sol. The structure-direction controlled by macro-molecular self-assembly undergoes a high-temperature calcination step, resulting in an inorganic material that resembles the polymer microphase morphology [80].

Commonly the used organic templates are amphiphilic poly(alkylene oxide) block copolymers, composed of two different polymers covalently connected at one end, such as triblock copolymers, $HO(CH_2CH_2O)_{20}(CH_2CH(CH_3)O)_{70}(CH_2CH_2O)_{20}H$ (designated $EO_{20}PO_{70}EO_{20}$, called Pluronic P-123) [81] and $HO(CH_2CH_2O)_{106}(CH_2CH–(CH_3)O)_{70}(CH_2CH_2O)_{106}H$ (designated $EO_{106}PO_{70}EO_{106}$, called Pluronic F-127) [79, 82]. Recently diblock polymers have also been used as structure-directing agents. Some examples include polystyrene-block-poly(4-vinylpyridine) (PS-b-P4VP) [83, 84], polystyrene-block-poly(2-vinylpyridine) (PS-b-P2VP) [85], polystyrene-block-poly(ethylene oxide) (PS-b-PEO) [86, 87], poly(vinyl chloride)-g-poly(oxyethylene methacrylate) (PVC-g-POEM) [67], and poly(isoprene-block-ethylene oxide) (PI-b-PEO) [88]. Moreover, other organics including poly(dimethylglutarimide) (PMGI), hydroxyl styrene-based cross-linkable polymers [89], cetyltrimethylammonium bromide (CTAB) micelles [90], cellulose [65], sodium alginate [91] and polyethylene glycol (PEG) [40] are also employed to direct the formation of mesoporous TiO_2 for solar energy applications. Using such sol-gel process, electrodes can be prepared directly on Si or FTO substrates. Furthermore, the process is highly scalable because it can be performed at low temperatures without any expensive or complicated equipment.

Among the various new microstructured electrodes designed recently, three-dimensional (3D) photonic crystal electrodes (Fig. 3c) made from colloidal crystal templates or inverse opals (Fig. 3b) have been well investigated due to their unique advantages [92, 93]. Photonic crystal (PC) materials exhibit periodicities in their refractive index on the order of the wavelength of light, and thus provide many interesting possibilities for “photon management” [94, 95]. Bragg diffraction in a periodic lattice, localization of heavy photons near the edges of a photonic band gap, multiple scattering at disordered regions in the photonic crystal, and the formation of multiple resonant modes are some of the phenomena that are exhibited by photonic crystals and can greatly enhance the effective light path within the active layer [68, 96]. 3D photonic colloidal crystals are of particular interest for enhancing light harvesting in DSSCs because these TiO_2 crystals can be both porous and significantly enhance light-matter interactions on the long wavelength side of the stop band. More importantly, the 3D ordered porous electrode with relatively large porosity is beneficial in applications that include polymeric electrolytes with high viscosities and relatively large molecular weight. Furthermore, 3D connected TiO_2 networks can provide an organized electron path, which may facilitate charge transport and thus enhance the collection efficiency of back-contact electrodes [72, 92]. In this regard, several hard templates, such as polystyrene (PS) [97, 98], poly(methyl methacrylate) (PMMA) [73], and SU8 photoresist [72] can be used to build the 3D backbone.

Interestingly, some designs are created using two kinds of templates. For example, a double layer couples a high surface area mesoporous anatase underlayer prepared using PI-b-PEO block polymer as template, with an optically and electrically active 3D periodic TiO_2 PC overlayer reversed from a PS template. Such a design is expected to allow effective dye sensitization, electrolyte infiltration, and charge collection from both the mesoporous and the PC layers, which acts as the photoanode in DSSCs [68]. Additionally, mesoscale colloidal PS particles and lithographically patterned SU8 macropores can be used as the dual templates, with the colloidal particles assembled within the macropores. The as-prepared template produces hierarchical TiO_2 electrodes for DSSCs with sufficient surface area from mesoscale pores and effective light scattering from micropores [99].

Alongside the effective organic templates, several inorganic materials including porous anodic alumina (PAA) [100], ZnO [101], $Cd(OH)_2$ [102] and SiO_2 [103] have been successfully employed as templates to construct TiO_2 architectures, such as ordered nanowires/nanotubes, mesoporous hollow spheres, and hierarchical nanoplates. One of the most commonly used templates, a PAA membrane with high density and high aspect ratio pores, is prepared by anodic oxidation of an aluminum sheet in a solution of sulfuric, oxalic, or phosphoric acids. It is frequently used as a template in nanowire or nanotube array synthesis through the sol–gel process described in Sect. 2.2.2 [104]. The PAA allows nanowires or nanotubes to grow on transparent conducting indium tin oxide (ITO) substrates without bending or breaking. This technique is capable of achieving a surface roughness factor equal to a typical nanoparticle layer [100]. In particular, a number of hybrid templated processes have been developed to construct attractive TiO_2 nanostructures. For example, 3D interconnected nanoporous TiO_2 nanotube arrays on fluorine-doped tin oxide (FTO) glass were prepared using a sol-gel process assisted by PVC-g-P4VP block copolymer and a ZnO nanorod template [105]. An organic–inorganic hybrid template (Fig. 4), Al_2O_3-POEM, is specially designed to fabricate a crack-free, organized mesoporous TiO_2 photoanode with high surface area, good interconnectivity, and uniform pores, yielding a high energy conversion efficiency of 7.3 % in DSSCs [78]. Other synthesis methods have also been assisted by templates, including hydrothermal [106, 107], atomic layer deposition (ALD) [108–110], microwave, and sonochemical methods [77].

2.1.2 Hydrothermal/Solvothermal Method

The hydrothermal/solvothermal methods have also been used to prepare a variety of TiO_2 nanomaterials [111–113]. In such processes (Fig. 5), the synthesis reaction generally occurs in aqueous/organic solutions containing required material precursors within temperature controlled steel pressure vessels called autoclaves. The reaction temperature can be raised above the boiling point of the water/organic solvent, reaching the pressure of vapor saturation. The temperature and the amount of solution added to the autoclave largely affect the internal pressure produced. The solvothermal method is almost identical to hydrothermal method except that

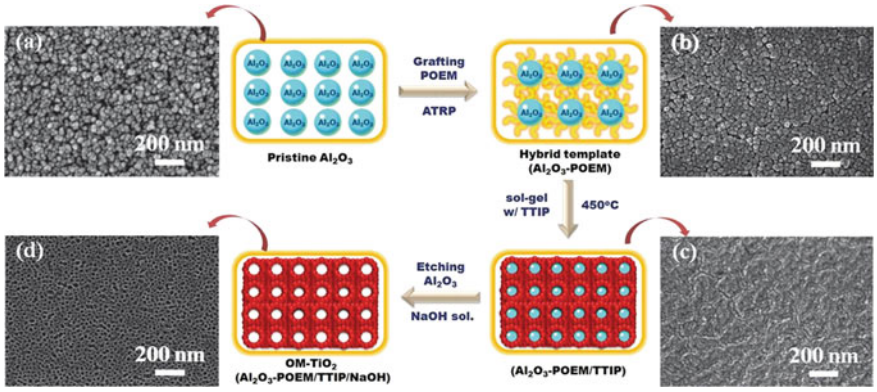

Fig. 4 Schematic of the preparation of the TiO_2 electrodes using hybrid templates. (Reprinted with permission from Ref. [78]). Copyright © Wiley-VCH

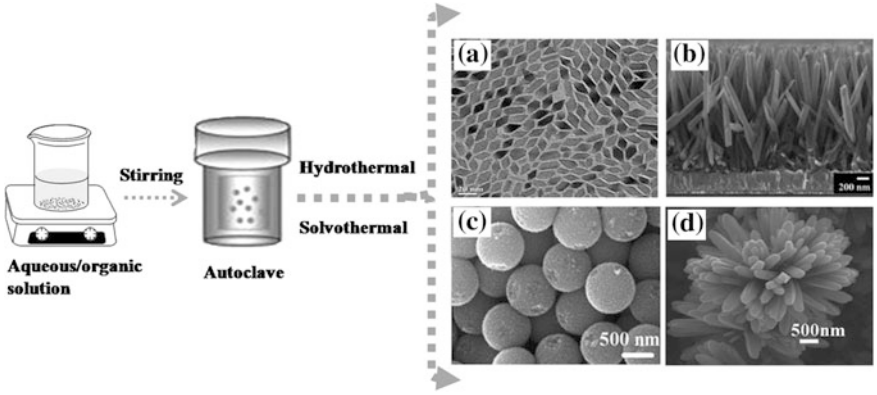

Fig. 5 Simplified schematic of hydrothermal and solvothermal synthesis and some typical structures prepared by both process: **a** nanosheets, **b** nanorods, **c** hollow microspheres and **d** flower-like microspheres. (Reprinted with permission from Ref. **a** [114], **b** [122], **c** [8] **d** [125]. Copyright © American Chemical Society and Wiley-VCH)

the solvents used for solvothermal synthesis are nonaqueous, while water is the primary hydrothermal solvent [114, 115]. Accordingly, the temperature in solvothermal process can be increased much higher than that in hydrothermal method because a variety of organic solvents with high boiling points can be adopted. Normally, the solvothermal method possesses better control over the size, structure, size distribution, and degree of crystallinity of TiO_2 nanomaterials compared to hydrothermal method [35].

In comparison with other methods, hydrothermal/solvothermal synthesis is a facile route to prepare a highly crystalline oxide under moderate reaction conditions, including low temperature (in general less than 250 °C) and relatively short

reaction time. It provides a convenient and effective reaction environment for the formation of nanocrystalline TiO_2 with high purity, good dispersion, and well-controlled crystallinity [116]. By employing this method, the calcination process, which is essential to the TiO_2 transformation from amorphous phase to crystalline phase, can be eliminated. Similarly, by tuning the hydrothermal conditions (such as temperature, pH, reactant concentration, molar ratio, and additives), crystalline products with different compositions, sizes, and morphologies can be achieved [117]. Many high-performance TiO_2 nanostructures, including novel nanocrystals [114], nanosheets (Fig. 5a) [22], 1D morphologies (e.g., nanotubes, nanowires, nanorods (Fig. 5b)) [118–122], mesoporous structures (Fig. 5c) [116, 123], and especially 3D hierarchical architectures (Fig. 5d) [29, 115, 124, 125] have been extensively developed via cost-effective hydrothermal/solvothermal methods and widely applied in DSSCs, H_2 generation and photocatalysis.

Recently, anatase TiO_2 single-crystalline nanosheets (NSs) with a high percentage of reactive (001) facets have attracted much attention as a dominant source of active sites for various applications such as photovoltaic cells, photodegradation of organic molecules, and photocatalytic water splitting [112, 126, 127]. Both theoretical and experimental studies indicate that the anatase TiO_2 (001) facets in particular are more reactive than (101) facets, which could be mainly attributed to different coordination numbers of Ti in (001) and (101) facets. In the (001) facets, each Ti atom coordinates with five oxygen atoms (i.e., with 100 % five-coordinate Ti (Ti_{5c}) atoms). While in the (101) facet, each Ti atom is coordinated with either five or six oxygen atoms with a 50 % probability for either case. Thus, the (001) facets display an enhanced number of oxygen vacancies in comparison with the (101) facets owing to the low coordination number of Ti with oxygen [128, 129]. However, anatase TiO_2 crystals are usually dominated by (101) facets, which are thermodynamically stable due to their lower surface energy than that of (001) facets (i.e., surface energy: $\gamma(001) = 0.90$ J/m^2 $> \gamma(100) = 0.53$ J/m^2 $> \gamma(101) = 0.44$ J/m^2). Consequently (101) facets account for more than 94 % of the total exposed surface according to the Wolff construction [4].

An important breakthrough in the preparation of anatase TiO_2 sheets with exposed (001) facets was achieved by Yang et al. in 2008. The synthesis of anatase TiO_2 single crystals with 47 % exposed (001) facets was realized by using hydrofluoric acid (HF) as a shape controlling agent to stabilize the (001) facets (Fig. 6a–c) [130]. Thereafter, numerous studies have been conducted toward the preparation and application of different shaped anatase TiO_2 micro- or nanocrystals with exposed (001) facets [131–133]. For example, Zheng et al. demonstrated a simple solvothermal synthesis, where tetrabutyltitanate, $Ti(OBu)_4$, was mixed with absolute ethanol and 40 % hydrofluoric acid solution, to produce TiO_2 microspheres assembled of anatase TiO_2 nanosheets with 83 % dominant (001) facets (Fig. 6d). These TiO_2 microspheres exhibited excellent photocatalytic activity for the degradation of methyl orange (MO) as shown in Fig. 6e [134]. Yang et al. demonstrated controllable hydrothermal synthesis of ultra-thin TiO_2 NSs with a thickness of only 1.6–2.7 nm and up to 82 % (001) facet coverage. It is found that the concentration of HF used as a capping agent significantly affected the thickness and side length of the

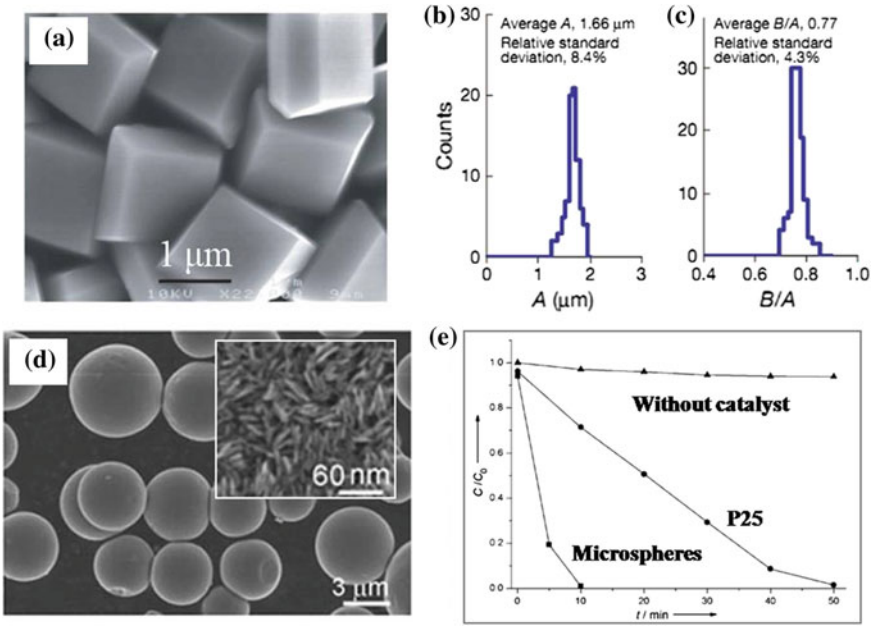

Fig. 6 SEM images of anatase single crystals (**a**) and TiO_2 microspheres composed of nanosheets with (001) facets (**d**), *inset* is the magnified surface of a microsphere. **b** The size distribution of anatase single crystals in (**a**). **c** The degree of truncation (B/A, A and B denote lengths of the side of the bipyramid and the side of the square {001} 'truncation' facets, respectively) of anatase single crystals in (**a**). **e** The corresponding photodegradation of methyl orange (MO) of (**d**). (Reprinted with permission from Ref. **a–c** [130], **d**, **e** [134]. Copyright © Nature Publishing Group and Wiley-VCH)

resulting TiO_2 nanosheets. Due to the high percentage of reactive (001) facets, the synthesized NSs loaded with 1 wt% Pt from photochemical reduction of water in the presence of methanol as a scavenger showed a H_2 evolution rate of 7381 μmol h^{-1} g^{-1} under UV-vis light [22]. Xiang et al. reported that the flower-like TiO_2 microsphere films with about 30 % exposed (001) facets were directly synthesized on the Ti foil in a dilute aqueous HF solution by a simple one-pot hydrothermal process and exhibited tunable photocatalytic selectivity toward decomposition of azo dyes by modifying the surface of TiO_2 microspheres as well as by varying the degree of etching of (001) facets [133]. Zhang et al. synthesized anatase TiO_2 microspheres with exposed mirror-like plane (001) crystalline facets via a facile low-temperature hydrothermal method. The improved light harvesting efficiency, attributed to the superior light scattering ability of the TiO_2 microsphere film, gave such microsphere photoanodes better overall light conversion efficiency of 7.91 % in DSSCs, which is 1.2 times the overall efficiency (6.73 %) obtained from the P25 photoanode [135].

Most of the hydrothermal syntheses reported so far have been carried out in the acidic environment with the addition of concentrated hydrofluoric acid, which is

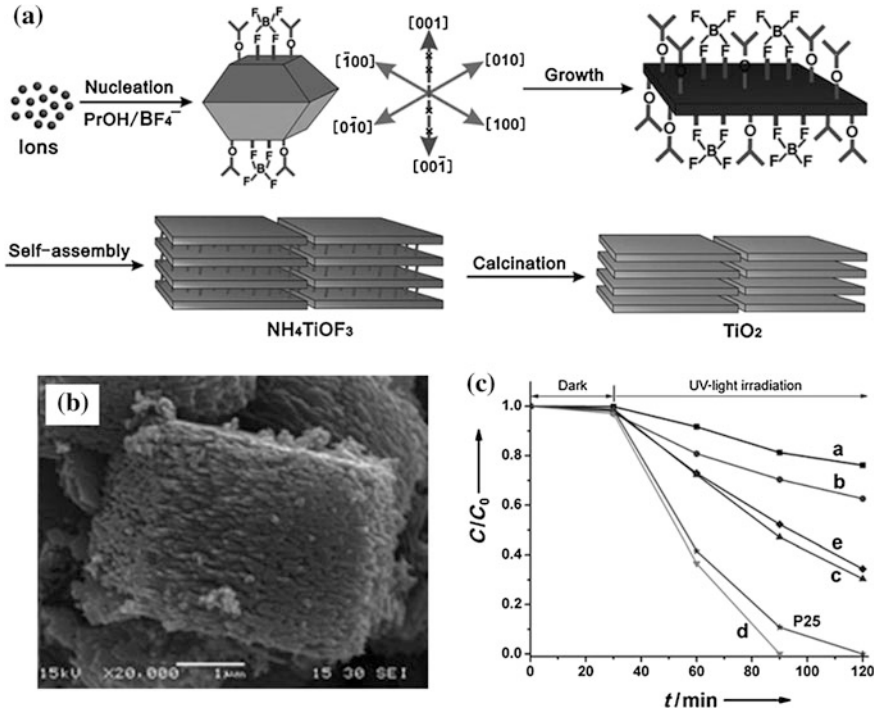

Fig. 7 **a** Schematic illustration of the formation mechanism for layered TiO_2. **b** SEM images of layered TiO_2 produced via the (**a**) process. **c** Photodegradation curves of RhB (20 mgL^{-1}) under UV-light irradiation over the TiO_2 samples prepared in different concentrations of 2-propanol (PrOH): a: 0, b: 1.5, c: 2.8, d: 4.0, and e: 8.0 M. (Reprinted with permission from Ref. [140]. Copyright © Wiley-VCH)

highly toxic and corrosive in both liquid and vapor forms [136]. In response to the safety and health concerns, a number of studies have investigated the preparation of anatase TiO_2 single crystals with clean and exposed (001) facets via hydrofluoric acid-free processes [137–139]. Recently, Yu et al. reported the synthesis of a layered TiO_2 structure composed of several nanosheets with exposed (001) facets, by a simple hydrothermal method in the presence of $(NH_4)_2TiF_6$, H_3BO_3, and 2-propanol, followed by calcination treatment (Fig. 7a). The resulting layered TiO_2 with (001) facet nanosheets (Fig. 7b) exhibited excellent photocatalytic activity for the degradation of rhodamine B (RhB) (Fig. 7c) [140]. Fang et al. synthesized submicrometer-sized yolk@shell hierarchical spheres composed of a permeable shell self-assembled by ultrathin anatase TiO_2 NSs with nearly 90 % exposed (001) facets and a mesoporous inner sphere with a high specific surface area. This process used the solvothermal method in the presence of diethylenetriamine (DETA), isopropyl alcohol (IPA) and titanium (IV) isopropoxide (TTIP), also followed by calcination treatment. Compared to the conventional (001) faceted TiO_2 NSs (4.01 %) and standard Degussa P25 (4.46 %), such anatase TiO_2

yolk@shell hierarchical sphere photoanodes (6.01 %) showed higher overall light conversion efficiency (η) for DSSC applications mainly due to their large surface area (up to 245.1 $m^2\ g^{-1}$) and their promotion of light scattering in the visible region using submicrometer scale features [113]. Han et al. presented the fabrication of truncated tetragonal bipyramidal TiO_2 nanoparticles with 60 % exposed (001) facets via a fluorine-free hydrothermal route, using potassium titanate nanowires as a precursor and urea as surface regulator [141]. Notably, Miao et al. prepared anatase TiO_2 microspheres with >90 % exposed (001) facets using TiF_4 as capping and stabilizing agent without introducing any additional hydrofluoric acid. Due to the high exposure of reactive (001) facets, the anatase TiO_2 microspheres gave an efficient photocatalyst in degrading methyl orange (MO) and producing hydrogen from water under UV light irradiation [142]. Similarly, Yang et al. fabricated hierarchical TiO_2 spheres made of thin nanosheets with over 90 % exposed (001) facets via a diethylene glycol-solvothermal route, which were used as photoanodes for DSSCs, and gave an energy conversion efficiency of 7.51 % [112].

Along with hydrothermal/solvothermal methods, other strategies have been investigated for the green preparation of highly reactive TiO_2 nanomaterials with exposed (001) facets [143]. Amona et al. found that faceted decahedral single-crystalline anatase particles with reactive (001) facets could be fabricated by a gas-phase process using $TiCl_4$ as a titanium source and that such a structure possessed comparable photocatalytic activity to that of P25 for reactions performed under various conditions [144]. Jung et al. presented the preparation of TiO_2 NTs with exposed (001) facets by electrochemical anodization of Ti foil using surfactant-assisted processes with poly(vinyl pyrrolidone) (PVP) and acetic acid. The DSSC assembled using a TiO_2 nanotube photoanode with 77 % exposed (001) facets demonstrated an overall conversion efficiency of 3.28 % [145]. Xie et al. developed a solid-state precursor strategy for preparing a hollow anatase TiO_2 box-like structure enclosed by six single-crystalline TiO_2 plates with highly exposed reactive (001) facets by sintering a cubic $TiOF_2$ solid precursor at 500–600 °C. The formation of these particular nanostructures is attributed to the hard self-template restriction and the adsorption of F^- ions from the $TiOF_2$. Due to the high percentage of reactive (001) facets, such novel TiO_2 boxes exhibited good performance in photocatalytic H_2 evolution (7.55 mmol $g^{-1}\ h^{-1}$) [146].

Furthermore, in addition to exposed (001) facets, TiO_2 nanocrystals with other important active facets have also been studied recently. For example, single crystalline anatase TiO_2 rods with dominant reactive (010) facets (also with 100 % five-coordinate Ti (Ti5c) atoms) were directly synthesized by hydrothermally treating $Cs_{0.68}Ti_{1.83}O_4/H_{0.68}Ti_{1.83}O_4$ particles. The nano-sized rods showed a 7.73 % conversion efficiency in DSSCs. This was comparable to the 7.67 % benchmark for P25 TiO_2 nanocrystals [147]. The preparation of tetragonal faceted-nanorods of single-crystalline anatase TiO_2 with predominately exposed higher energy (100) facets was performed by hydrothermal transformation of sodium titanate in alkaline solution [138]. Significantly, anatase TiO_2 nanocuboids wholly exposed with high-energy (001) and (100) facets were successfully synthesized by an environmentally benign synthetic strategy using low-cost acid-delaminated vermiculite (DVMT)

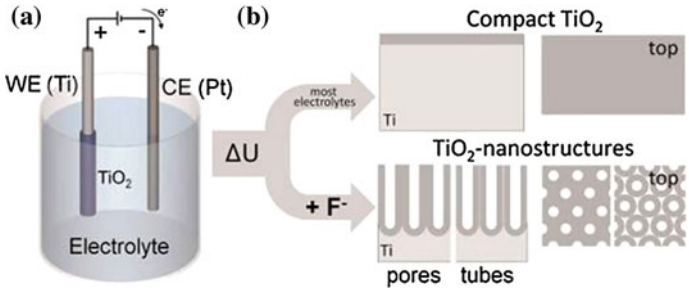

Fig. 8 **a** Schematic diagram of anodization experiments. **b** Anodization leads to the formation of a compact oxide on Ti (in most neutral and acidic electrolytes). If dilute fluoride electrolytes are used, highly ordered nanoporous or nanotubular anodic oxide layers can be formed. In the case of nanoporous oxide, the layer consists of vertically aligned nanosized channels in an oxide matrix while in the case of nanotubular morphology the layer is composed of an ordered array of oxide nanotubes. (Reprinted with permission from Ref. [150]. Copyright © Wiley-VCH)

and tetramethylammonium hydroxide (Me_4NOH) as synergistic morphology-controlling reagents [148]. In contrast to anatase TiO_2 with low-index facets like (101), (001), and (100), recently Li et al. reported the fabrication of an anatase TiO_2 nanosheet array assembled by (116) facet-oriented nanocrystallites. The (116) facets were made parallel to the surface of a FTO substrate via a two-step process, which exhibited 50 % higher photocatalytic activity than (001) facet-oriented nanosheet arrays in the degradation of methyl blue (MB) under UV light irradiation [149].

2.1.3 Electrochemical Anodization Method

Anodic oxidation represents a facile and well-established method to form nanostructures in a self-organiting way [104]. The controlled oxidation of titanium metal under electrochemical anodization provides another method of TiO_2 nanomaterial production [52]. In general, the anodization process is conducted in a two-electrode electrochemical cell at a constant potential in aqueous or organic electrolyte with Ti foil as an anode and platinum foil as a cathode (Fig. 8a) [150]. Under optimized anodized conditions, highly ordered nanoporous or nanotubular architectures with high aspect ratios could be successfully achieved [151]. Anodization is particularly useful in the synthesis of TiO_2 nanotubes from titanium foil. Anodization has been extensively studied after pioneering work in 2001 by Gong et al. in which they reported the formation of nanotubes up to 0.5 mm in length by electrochemical anodization of titanium foil in HF aqueous electrolyte [152].

Among the various forms of semiconductor nanostructures, one-dimensional (1D) highly ordered architectures, such as nanowires, nanorods, nanofibers, nanotubes with high surface area-to-volume ratios possess useful and unique properties compared to their bulk counterparts [39]. The highly ordered nature of

these 1D nanostructures gives them excellent electron percolation pathways for directional charge transfer between interfaces. For example, the mobility of electrons in 1D nanostructures is typically several orders of magnitude higher than in semiconductor nanoparticle films [153]. In comparison with other 1D morphologies, nanotubes provide a larger interfacial area due to their external and internal surfaces, which is beneficial for surface area-dependent applications [154]. Studies on TiO_2 have shown that vertically oriented nanotube arrays are remarkably efficient when applied in sensors, water splitting, DSSCs, and photocatalysis [155–160].

In the past decade, self-organized oxide nanotube arrays have attracted extensive scientific and technological interest. Thus, TiO_2 nanotube arrays have been synthesized by a variety of methods, including template deposition (e.g., AAO templates, ZnO nanorod templates, or organic templates) [161], electrochemical anodization [162], and hydrothermal techniques [163]. Among these, an inexpensive and straightforward approach that leads to well-behaved nanotubes is the anodization method, which enables precise control over the resulting tube diameter, tube length, and overall morphology by adjusting various parameters such as the pH, concentration and composition of electrolyte, applied potential, growth time, and temperature of the anodization process [164–167]. Interestingly, the addition of fluoride ions tends to control the overall development of nanotube architecture (Fig. 8b). There are several excellent reviews detailing the growth mechanism in anodic oxidation [168–171].

Normally, the anodization process can be divided roughly into three stages: (1) electrochemical oxidization of the titanium surface which results in the formation of an initial TiO_2 barrier layer, corresponding to the first current drop; (2) chemical etching of TiO_2 by F^- to form TiF_6^{2-}, resulting in nanotube formation that leads to a current increase; and (3) the growth of nanotubes, which results in a slow current decrease [172]. Briefly, the nanotube growth is determined by the equilibrium between anodic oxidation and chemical dissolution. The anodic oxidation rate is mainly controlled by the anodic potential, while the chemical dissolution rate is controlled by the electrolyte acidity and F^- concentration [173]. As previously mentioned, since the discovery by Gong and co-workers in 2001, TiO_2 nanotube fabrication has been intensively investigated over the past decade. Consequently, a variety of nanotubular architectures have also been explored. In particular, by varying the voltage during the growth, new self-organized TiO_2 morphologies could be obtained: bamboo-type nanotubes [174], branched nanotubes [175], periodic nanotubes [176], ridged nanotubes [177], double-walled nanotubes [178], and multilayer nanotubes [179]. In the following sections, some representative fabrication processes developed recently for high-performance photovoltaic applications are discussed in greater detail.

TiO_2 nanotubes prepared via anodization of Ti foil are attached to the Ti substrate with closed bottom. In most cases, the use of Ti foil leads to TiO_2 nanotube arrays supported on Ti substrate. However, in many applications, detached TiO_2 nanotube layers are required. TiO_2 nanotube arrays grown in situ on opaque titanium foil are difficult to apply to high-efficiency DSSCs because the

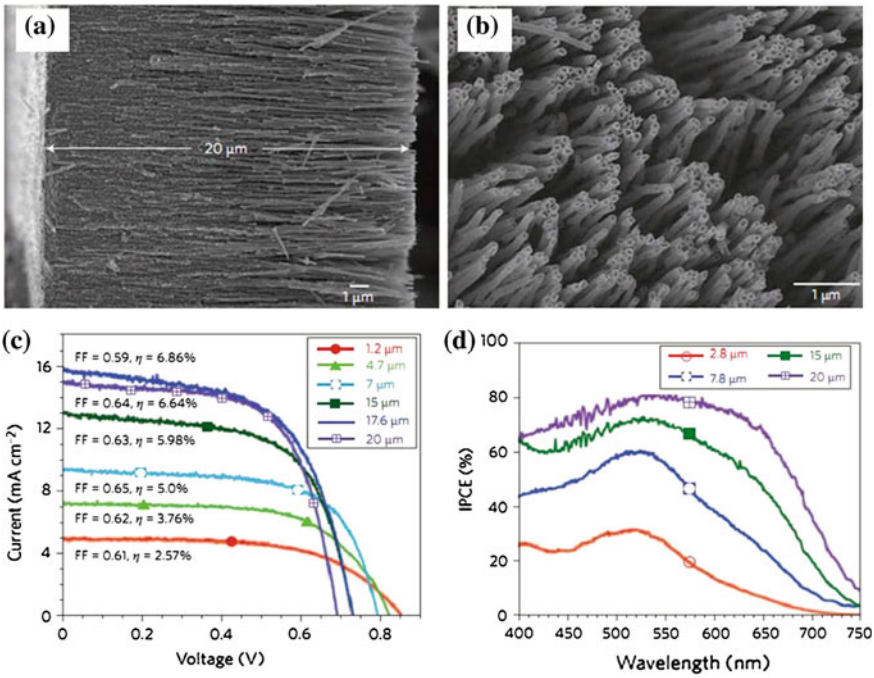

Fig. 9 SEM images of a 20-μm-long TiO_2 nanotube array from anodization of the Ti film sputter-deposited on FTO-coated glass: **a** cross-sectional view and **b** top view. The current-voltage characteristics (**c**) and the incident photon-to-current conversion efficiency (IPCE) spectra of DSSCs fabricated using transparent nanotube array films of various lengths. (Reprinted with permission from Ref. [188]. Copyright © American Chemical Society)

incoming light using back illumination mode is partially reflected by the counter electrode and partially absorbed by the counter electrode and iodine in the electrolyte before striking TiO_2 nanotubes, leading to a loss of ~25 % of the incident solar energy [180]. Furthermore, sintering of the TiO_2 for transformation from amorphous phase to crystalline phase (i.e. anatase or rutile) can introduce the formation of a barrier layer between the nanotubes and the underlying Ti substrate. This enables recombination of electrons and holes when the nanotube layers are used for photoelectrochemical water splitting [181]. Fortunately, several strategies have been explored to solve this deadlock. One straightforward alternative solution is to deposit titanium as a thin film on a transparent substrate (e.g., FTO glass) before anodizing. The deposition process is usually performed by physical methods, for example, radio-frequency (RF) or direct-current (DC) magnetron sputtering [182–187]. Through anodization of sputtered titanium into nanotube layers on transparent substrate (Fig. 9a, b), a power conversion efficiency of 6.9 % for the resulting DSSCs was obtained (Fig. 9c, d) [188]. The length of the nanotubes is limited by the difficulty of growing a high quality, thick Ti film on the conductive glass via sputter deposition [189]. Therefore, a large-area free-standing

TiO_2 nanotube film with tunable tube lengths was developed by a two-step anodization process and then transferred onto FTO glass via a layer of TiO_2 nanoparticle paste [190–195]. This process, however, results in closed-bottom tube-ends. This is problematic because the interface between the TiO_2 nanotube arrays and the TiO_2 nanoparticle layer might cause near-UV light absorption and front surface light reflection and block the diffusion of the redox reagents into the underlying TiO_2 nanoparticles coating on the collecting FTO substrate. Thus, a number of methods have been developed to fabricate free-standing TiO_2 nanotube arrays, including critical point drying, dissolution of the Ti substrate in water-free CH_3OH/Br_2 solution, solvent evaporation, ultrasonic agitation, chemically assisted delamination and potential shock [196–201]. For example, Li et al. removed the caps of the closed-bottom TiO_2 nanotubes by immersing the as-prepared free-standing TiO_2 nanotube film in an oxalic acid solution. As compared to the closed-end TiO_2 nanotube-based DSSC, the opened-end TiO_2 nanotube-based device exhibited an increase in one-sun efficiency from 5.3 to 9.1 %, yielding a 70 % enhancement [202].

A novel version of DSSCs was introduced to overcome the light illumination problem of TiO_2 nanotube-based electrodes, namely, three-dimensional dye-sensitized solar cells (3D DSSCs). In this system titanium wires or meshes are utilized instead of titanium foils or sheets to fabricate TiO_2 anodized nanotubes [203–208]. Misra et al. used a TiO_2 nanotube-based wire as a working electrode (Fig. 10a–c) and a platinum wire as a counter electrode in a DSSC. This DSSC achieved a conversion efficiency of 2.78 % under AM 1.5 simulated solar light (Fig. 10d). The prototype device is capable of achieving long distance transport of photo-generated electrons and multi-directional light harvesting from surrounding to generate electricity [205]. Wang et al. developed a new type of 3D DSSCs with double deck cylindrical Ti meshes as the substrates. Here, one of the Ti meshes was anodized to in situ synthesize the self-organized TiO_2 nanotube layer to serve as the photoanode. Another Ti mesh was platinized through electrodeposition as the counter electrode. This all-Ti 3D DSSC exhibited the highest conversion efficiency of 5.5 % under standard AM 1.5 sunlight [204].

In addition, vertically ordered TiO_2 nanotube arrays also face the serious problem of insufficient surface area due to the large diameter of nanotubes and considerable free space between nanotubes. This leads to poor dye adsorption capacity when applied in DSSCs [209]. In light of this limitation, many strategies have been explored [46, 103, 210–212]. For example, a common combination of TiO_2 nanotubes and nanoparticles was realized by treating the as-anodized nanotubes with a $TiCl_4$ solution which hydrolyzed to yield nanoparticles. This can increase the nanotube surface area and bridge any cracks resulting from annealing, and thus improve the conversion efficiency of nanotube-based DSSCs [213, 214]. Recently, novel hierarchical-structured TiO_2 nanotube arrays have been prepared by combining the two-step electrochemical anodization with a hydrothermal process. The resulting DSSCs exhibited good performance and applicability [212].

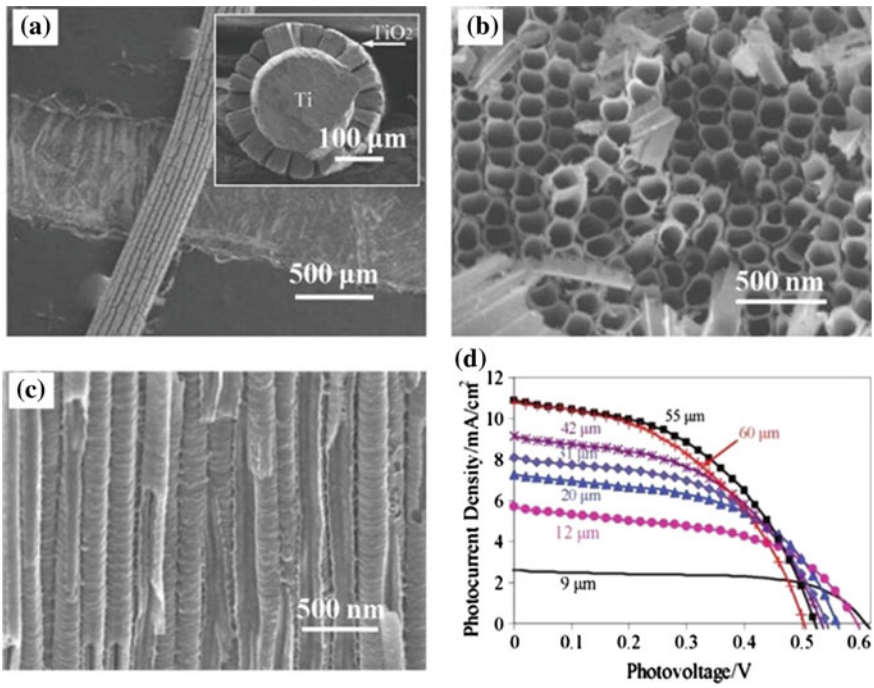

Fig. 10 SEM images of TiO_2 nanotube arrays grown around a Ti wire: Top view (**a**), *inset* is cross-sectional view, magnified top view (**b**) and magnified cross-sectional view (**c**). The current–voltage characteristics (**d**) of DSSCs using TiO_2 nanotube arrays with different lengths. (Reprinted with permission from Ref. [205]. Copyright © American Chemical Society)

2.1.4 Electrospinning and Electrospray Methods

Electrospinning is a simple and versatile nanofabrication technique for preparing several continuous 1D nanofibers, including polymers, ceramics, composites and metals, with controllable diameters ranging from a few nanometers to several micrometers [215, 216]. Electrospinning works using the principle of asymmetric bending of a charged liquid jet accelerated by a longitudinal electric field (Fig. 11) [217]. A diversity of soluble and fusible polymers (e.g., polyvinylpyrrolidone (PVP), polyacrylonitrile (PAN), polyurethane (PU) and polyvinyl acetate (PVAc)) can be electrospun to form nanofibers from their precursor solutions [218, 219]. If the polymeric solution contains the inorganic precursors (e.g., TiO_2, SnO_2 and ZnO), organic/inorganic composite nanofibers are obtained. These are subsequently calcinated at high temperature to thermally decompose organic components, and produce inorganic nanofibers with minimal morphological change [135, 220]. The diameter, alignment, and morphology of these nanofibers can be tailored by controlling the liquid injection rate, intensity of the electric field, and shape of the collector surface, respectively. The diameter of nanofibers also depends on the intrinsic properties of the polymeric solution such as the viscosity and surface charge.

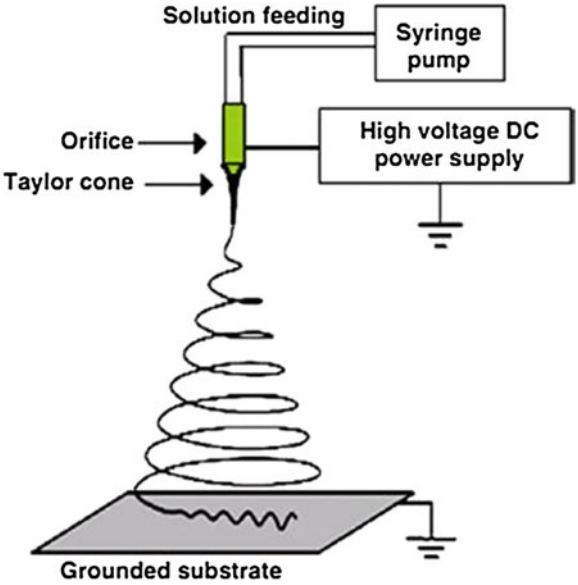

Fig. 11 Schematic diagram of electrospinning method. (Reprinted with permission from Ref. **a** [218]. Copyright © Institute of Physics Publishing)

After the first report of electrospun TiO_2 nanofibers in 2003 [221], many studies have been performed for applications in photovoltaic devices and photocatalysis since the electrospun nanofibers can be fabricated with controllable size, density, and orientation [222, 223]. More importantly, electrospinning is simple, controllable, inexpensive, and scalable for industrial production [224]. For instance, Yang et al. prepared a bi-layer TiO_2 nanofiber photoanode via combining both small and large-diameter TiO_2 nanofibers in the nozzleless electrospinning by changing the applied voltage, electrode separation distance, and electrospinning time. It is expected that the smaller-diameter nanofiber layer with a high surface-to-volume ratio can load enough dye molecules and directly transport electrons within the 1D channels. While the larger-diameter nanofiber layer can serve as a light scattering layer, further adsorbing more dye molecules, and even providing higher porosity to facilitate electrolyte diffusion. With the bi-layer photoanode, the efficiency (η) of DSSCs can be improved from 7.14 % for the single-layer to 8.40 % for the bi-layer TiO_2 nanofiber photoanode [225]. As shown in Fig. 12a, multi-scale porous TiO_2 nanofibers were fabricated from HF etching of TiO_2/SiO_2 composite nanofibers, which were electrospun from a hybrid solution of dissolved SiO_2 colloidal solution, TTIP and PVP, followed by calcination. Such fiber-based DSSCs showed an η of 8.5% (Fig. 12b), which is greater than those of conventional photoelectrodes made of TiO_2 nanoparticles (6.0 %) [226].

Other useful structures, including nanorods [227], rice-like shapes [228], and hollow fibers [229], have been derived from electrospinning methods. TiO_2 nanorod-based photoelectrodes (Fig. 12c) were prepared by sintering TiO_2 composite nanofibers that were electrospun from a solution mixture of TiO_2 sol-gel and

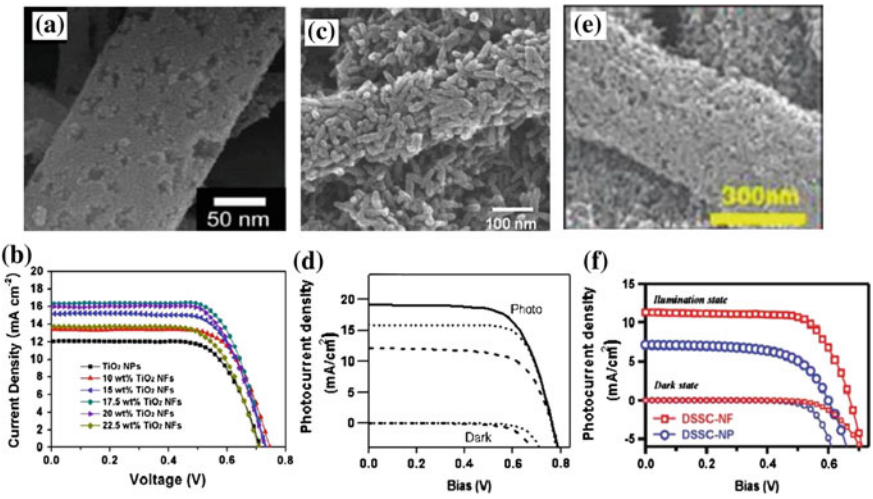

Fig. 12 SEM images of TiO_2 multi-scale porous nanofibers (**a**), electrospun nanorods (**c**) and hierarchically structured nanofibers (**e**). The current–voltage characteristics (**b**, **d**, **f**) of DSSCs based on (**a**, **c**, **e**), respectively. (Reprinted with permission from Ref. **a**, **b** [226], **c**, **d** [230], **e**, **f** [233]. Copyright © American Chemical Society)

PVAc in dimethyl formamide (DMF). The efficiency of such nanorod-based DSSCs was optimized to achieve 9.52 % under masked illumination of simulated solar light, AM 1.5 Global (Fig. 12d) [230]. Rice grain-shaped TiO_2 films were produced by 500 °C calcination of the nanofibers prepared from electrospinning [231]. The photovoltaic and photocatalytic performance of the rice grain-shaped structures are superior to commercially available P25 [232]. Furthermore, it has also been demonstrated that the rice grain-like structures are also superior to the nanofibers in scattering light with a 15.7 % enhancement in efficiency compared to 9.63 % for nanofibers [228]. Attractive hierarchical structures can also be obtained from a combination of electrospinning and other powerful methods, such as hydrothermal processes [214]. Hierarchically structured TiO_2 nanofibers prepared from electrospinning followed by a stepwise calcination treatment exhibited a unique morphology in which microscale core fibers were interconnected and numerous nanorods were deposited onto the fibers (Fig. 12e). This nanorod-in-nanofiber morphology possessed high porosity at the mesopore and macropore levels, facilitating the infiltration of plastic crystal electrolytes in DSSCs and yielding an optimized η up to 7.93 % (Fig. 12f) [233]. In addition, a hierarchically heterostructured TiO_2 nanocomposite composed of rutile nanosheets standing perpendicular on anatase nanofibers, can be successfully prepared through a combination of electrospinning and solvothermal processes [26].

Recently, the electrostatic spray (e-spray) technique has attracted a lot of attention because it is a simple, versatile, and cost-effective technology that can be applied in a variety of fields for the fabrication of semiconductive ceramics,

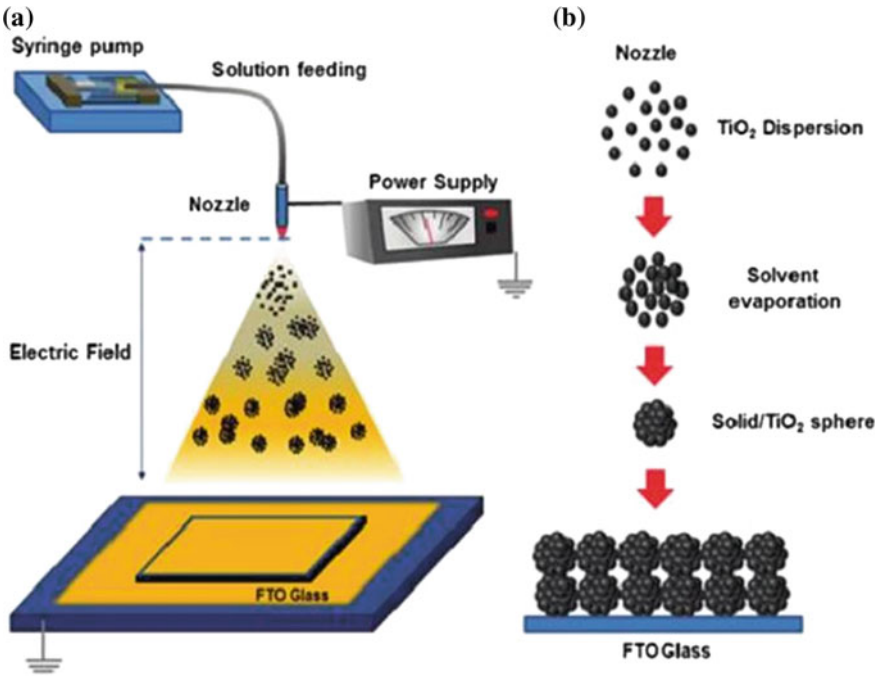

Fig. 13 **a** Schematic diagram of electrostatic spray and **b** formation of hierarchically structured TiO_2 nanospheres by electrostatic spray. (Reprinted with permission from Ref. **a**, **b** [59]. Copyright © American Chemical Society)

polymer coatings, protein films, and micro-patterns [234, 235]. In the electrospray process, a jet of liquid is sprayed toward a collector under a strong electric field (Fig. 13a). During e-spray deposition, known as induction or conduction charging, the droplets can be charged and atomized by mechanical forces in the presence of electric field between the solution and the depositing substrates. The electric field provides an electric charge on the liquid surface and the charge is carried out by the droplets detaching from the jet. The deposition efficiency of the charged droplets is usually higher than that of the uncharged droplets, which can improve the adhesion between the materials and substrates (Fig. 13b) [59]. In brief, three parameters typically determine the structures created by the electrospray method: (1) solution conditions such as the solvents and precursors, (2) processing conditions such as applied voltages, distance between the tip of the needle and collector and flow rates, and (3) ambient conditions such as temperature and humidity [235, 236]. As a deposition technique, e-spray has many advantages, such as large treatment areas, compatibility with various substrate geometries, and high deposition rate. Moreover, electrospray devices can perform at room temperature under atmospheric pressure, making it an energy efficient and low-cost technology [237].

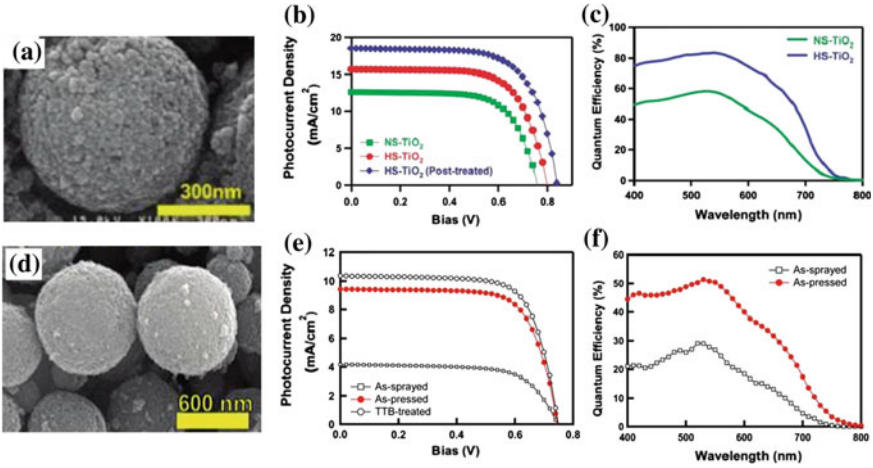

Fig. 14 SEM images of hierarchically structured TiO_2 microspheres (**a**, **d**). The current–voltage characteristics and IPCE spectra of DSSCs (**b**, **c**), and flexible DSSCs (**e**, **f**) based on the TiO_2 microspheres. (Reprinted with permission from Ref. **a**–**c** [59], **d**–**f** [240]. Copyright © American Chemical Society)

Accordingly, e-spray could be a promising method for the preparation of photoanodes for the industrial-scale manufacture of DSSCs. Based on reported works, several significant TiO_2 nanostructures including hierarchically structured mesoporous spheres, hollow hemispherical aggregates, and nanoflakes have been developed using electrospray methods [211, 236, 238]. Of these structures, mesoporous spheres are the most advantageous on account of their large surface areas for abundant dye loading, high porosity for efficient electrolyte diffusion, and microscale framework for effective light scattering [59]. In comparison with other methods (e.g., hydrothermal/solvothermal process) for the preparation of mesoporous TiO_2 spheres, e-spray is advantageous because this technique can directly realize the formation of aggregated spheres by purely physical force, regardless of chemical composition and surface chemistry (Fig. 13b) [235]. Moreover, it has inherent flexibility in controlling the diameter and diameter distribution of the spheres by simply tuning the electrospray parameters, such as the feeding rate and the applied voltage [238, 239]. In addition, e-spray facilitates the adjustment of stacking density and porosity of the spheres on substrates through the proper selection of polymer additives [239]. For example, Hwang et al. have performed an extensive study on the fabrication of hierarchically structured mesoporous TiO_2 spheres by e-spray method (Fig. 14a, d), and further applied such photoanodes in solar cells, achieving efficiency as high as 10.57 % for DSSCs (Fig. 14b, c) [59], 5.57 % for flexible DSSCs (Fig. 14e, f) [240], and 7.59 % for solid-state DSSCs [241], respectively.

2.1.5 Other Methods

Vapor deposition describes any process in which materials in a vapor state are condensed to form a solid phase material, usually conducted within a vacuum chamber. If no chemical reaction occurs, this process is called physical vapor deposition (PVD); otherwise it is called chemical vapor deposition (CVD) [20, 35]. In PVD, materials are evaporated followed by condensation to form a solid material. The primary PVD methods include thermal deposition, ion plating, ion implantation, sputtering, laser vaporization, and laser surface alloying [20, 35]. PVD is considered an effective method to fabricate uniform, high-quality semiconductors, especially composite and doped semiconductors. Moreover, PVD enables the formation of uniform nanostructured thin films, in which the size and shape can be precisely controlled [242]. Two versatile PVD methods, oblique angle deposition (OAD) and glancing angle deposition (GLAD), are based on the geometric shadowing effect, and are widely applied to prepare well-aligned nanorod arrays [243]. In OAD, the incident vapor flux is directed onto a substrate at a nonzero angle θ with respect to the substrate normal. When the vapor incident angle θ is large (i.e., $\theta > 70$), a well-defined nanorod array tilted toward the direction of the vapor flux can be obtained [244]. The GLAD method is similar to OAD in that it uses a large incident vapor angle, but the substrate is rotated azimuthally at a constant speed during the deposition. The result is vertically aligned nanorod arrays [245]. By changing the deposition parameters in these PVD methods, one can easily fabricate specific nanostructured porous array films such as cylinders, helices, spheres, and zigzags all with controllable surface areas [242, 243, 246, 247].

In addition, femtosecond and nanosecond pulsed laser deposition (PLD) at different wavelengths is also widely used to construct nanoparticle-assembled TiO_2 films. This technique is useful for controlling the dimensions and the crystalline phase of nanoparticles by varying the laser parameters and the deposition conditions. It is also suitable for depositing TiO_2 films at a high deposition rate and low cost [248–250]. Recently, a novel forest-like architecture consisting of hierarchical assemblies of tree-like nanocrystalline particles of anatase TiO_2, were grown on FTO substrates via pulsed laser deposition (PLD) at room temperature by ablation of a Ti target in a background O_2 atmosphere. The resulting architecture was proposed to be beneficial to reduce the electron recombination and also control mass transport in the mesopores, and thus achieved a 4.9 % conversion efficiency in a DSSC [251].

However, in CVD processes, thermal energy heats the gases in the coating chamber to induce the deposition reaction. Typical CVD approaches include electrostatic spray hydrolysis, diffusion flame pyrolysis, thermal plasma pyrolysis, ultrasonic spray pyrolysis, laser-induced pyrolysis, and atmospheric pressure and ultronsic-assisted hydrolysis [20, 35, 252, 253]. Several TiO_2 nanostructures prepared though CVD have been reported. For example, TiO_2 nanoparticles with sizes below 10 nm were prepared by pyrolysis of TTIP via CVD in a mixed helium/oxygen atmosphere [254]. TiO_2 nanorods were grown on a Si substrate using TTIP as the precursor by metal organic CVD (MOCVD) [64].

2.2 Modifications of TiO_2

As a promising semiconductor material, TiO_2 has attracted significant attention over the past several decades. However, the practical photovoltaic and photocatalysis applications of TiO_2 are limited by its wide band gap and the serious recombination of photogenerated electrons and holes [33, 34]. Because of its large band gap (3.2 eV for anatase, 3.0 eV for rutile), pure TiO_2 only absorbs ultraviolet light shorter than 387.5 nm for the anatase and 413.3 nm for the rutile [33]. Unfortunately, UV light constitutes less than 5 % of the solar energy that reaches the surface of the earth. This reduces the effective use of sunlight since visible light ($\lambda = 400$–700 nm) accounts for about 50 % of solar energy. Thus, it is necessary to develop titania-based photocatalysts which are active under visible light (i.e., broad spectrum). Furthermore, recombination of photogenerated charge carriers is another major limitation in TiO_2 semiconductor materials since it reduces the overall quantum efficiency of devices. In photocatalysis applications, recombination occurs when the excited electron reverts to the valence band without reacting with adsorbed species and the energy, non-radioactively or radioactively, dissipates as either light or heat [34]. However, in DSSC applications, photoexcited electron recombination in the electron transport process, including electron injection from the excited dye to the TiO_2 conduction band and electron transport from the conduction band to the conductive substrate, is regarded as one of the major obstacles to achieving high solar-to-electricity conversion efficiencies [255]. Recombination may occur either on the surface or in the bulk and is generally made worse by the presence of impurities, defects, and all other factors which introduce bulk or surface imperfections into the crystal.

To solve these problems, extensive efforts have been devoted to creating TiO_2-based visible-light-active photocatalytic materials and modifying nanostructured TiO_2 photoanodes to alleviate electron recombination [33, 256]. Currently, research interests focus mainly on modifying TiO_2 materials via (1) doping with cations (e.g., Fe [257–259], Cr [260], Eu [261], La [262], V [263], Mg [255], In [264]) or anions (e.g., S [265], C [266], F [267], B [268] and N [269]); (2) sensitization with organic dyes (e.g. N3, N719) [270], conducting polymers (e.g., poly(3-hexylthiophene) (P3HT) [271], nafion (perfluorinated polymer with sulfonate groups) [272, 273], polyaniline (PANI) [274], and carbon nitride polymer [275]), organic–inorganic hybrid dyes (e.g. copper(II) phthalocyanine) [276], or other semiconductors that absorb visible light (e.g. CdS [277–279], Cu_2O [280], Ag_2O [281], CdSe [282], $PbZr_{0.52}Ti_{0.48}O_3$(PZT) [283], Bi_2O_3 [284], BiOI [285], Bi_2WO_6 [286], CdTe [287], PbS [288], $CuInS_2$ [289], SnS [290], SnS_2 [291]); (3) decoration with noble metals (e.g. Au [292–294], Ag [65, 295–297], Pd [298–300], Pt [301–303]); (4) combination with other semiconductors (e.g., SiO_2 [304, 305], Al_2O_3 [100, 306], MgO [307], Fe_2O_3 [308], $SrTiO_3$ [309], Nb_2O_5 [310], SnO_2 [311], WO_3 [312], ZnO [313], and ZrO_2 [314]); and (5) synthesis of reduced TiO_2 (TiO_{2-x}, containing Ti^{3+} or O vacancies) [235, 315–318].

Among these methods, ion doping has been widely adopted to adjust the position of either the conduction band (CB) or valence band (VB) of TiO_2. This could have the desired effect of making the electrons excitable under visible light irradiation to produce photoelectron-hole pairs. The mechanism of the visible absorption is produced from interaction between the 2*p* orbitals of the dopant and the 2*p* orbitals of the oxygen in the newly formed valence band or the creation of dopant isolated states above the valence band maximum [319–321]. Nonmetal ion doping is usually considered more promising than metal ion doping because metal ion doping can introduce undesirable defects which can serve as the recombination centers for photoelectron–hole pairs, and thus reduce the pollutant degradation efficiency [322]. Nitrogen is the most promising dopant and can be easily introduced into the TiO_2 structures, due to its comparable atomic size with oxygen, small ionization energy and high stability [323]. Since Sato et al. found that the addition of NH_4OH to TiO_2 sol, followed by calcination of the precipitated powder, could generate a material which showed a visible light response, many strategies have been developed to produce N-doped TiO_2 materials [324, 325]. In the past decades, doping of nitrogen into TiO_2 structures has been realized via both wet and dry preparation methods. Physical techniques (i.e., sputtering and ion implantation) based on the direct treatment of TiO_2 with energetic nitrogen ions have also been developed [321, 326]. Meanwhile, gas phase reaction methods (i.e., atomic layer deposition and pulsed laser deposition) have been successfully used to prepare N-doped TiO_2 materials [269, 327]. The sol–gel method has proven to be the most versatile technique for the synthesis of N-TiO_2 nanoparticles because of its low cost, relatively simple equipment, and easy control of the resulting nanostructures [328]. In brief, the simultaneous growth of TiO_2 and N doping can be realized by hydrolysis of titanium precursors (i.e., titanium tetrachloride, titanium tetra-isopropoxide, tetrabutylorthotitanate) in the presence of nitrogen sources (i.e., aliphatic amines, nitrates, ammonium salts, ammonia, and urea) [328–330].

Recent studies have also revealed that doping TiO_2 with other elements, such as S, F, C, and B shifts the optical absorption edge to longer wavelengths [267, 331–333]. For example, F-doped flower-like TiO_2 nanostructures (Fig. 15a) have been synthesized in the presence of HF by a mild hydrothermal process and exhibited high photoelectrochemical activity for water-splitting and the photodegradation of organic pollutants (Fig. 15b) [334]. Mesoporous C-doped TiO_2 materials were prepared by a hydrothermal synthetic approach using sucrose as a carbon-doping source, followed by a post-thermal treatment. The resulting C-doped TiO_2 photocatalyst showed reduced recombination of electron–hole pairs due to the reduction of surface defects and promoted visible-light photocatalytic activity (Fig. 15c, d) [335]. In order to further improve the photocatalytic activity, co-doping TiO_2 with double non-metal elements (i.e., N–S [336], N–B [329, 337], F–N [338], C–N [339]) has attracted more attention. For example, F–N co-doped TiO_2 nanoparticles with dominant (001) facets were prepared by calcination a $TiOF_2$ precursor in NH_3 gas flow. The resulting nanoparticles showed drastically enhanced absorption and excellent water oxidation performance under visible light irradiation [338].

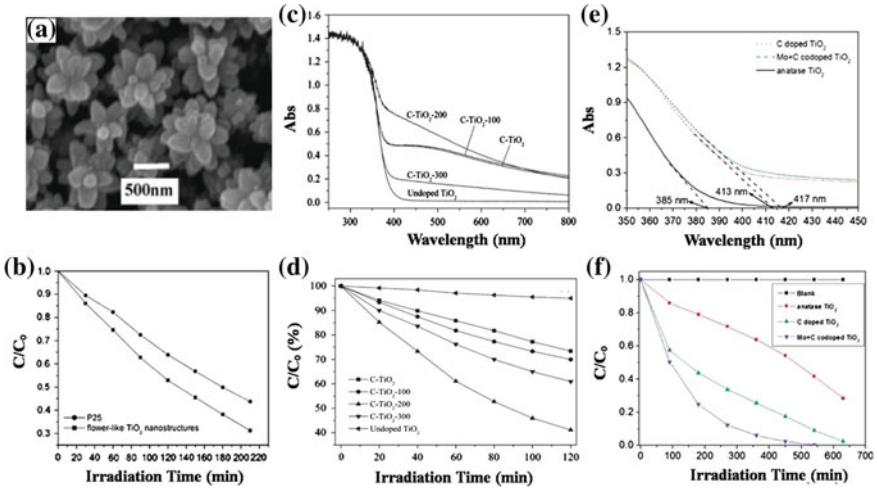

Fig. 15 SEM image of F-doped TiO_2 flowers (**a**). UV-visible absorption spectra of C-doped (**c**) and Mo, C-codoped TiO_2 (**e**), respectively. **b** The variation of 4-nitrophenol concentration by photoelectrocatalytic reaction with flower-like TiO_2 (**a**) and P-25. The visible light photocatalytic activities (**d**) of C-doped TiO_2 (**b**) treated at different temperatures in the degradation of gaseous toluene. Photodegradation of MB (**f**) by photochemical reaction with Mo, C–codoped TiO_2 (**e**). (Reprinted with permission from Ref. **a**, **b** [334], **c**, **d** [335], **e**, **f** [343]. Copyright © American Chemical Society)

It has been shown that nonmetal-doped TiO_2 shows a redshift of the onset and a higher absorption in the visible light spectrum. Metal doped TiO_2 would possess lower energy levels so that electrons and holes can be excited by low energy photons, which also increases the absorption of visible light [340]. For example, Mo–TiO_2 core-shell nanoparticles were prepared by the arc-discharge method and showed enhanced photocatalytic activity under visible light, due to the Mo-doping in (001) TiO_2 from diffusion at the shell–core interface [341], while many studies have revealed that single doping will increase recombination sites inside the TiO_2, which will therefore increase the charge recombination [260]. Conversely, it has also been demonstrated that co-doping TiO_2 with both nonmetal anions and metal cations can reduce the recombination sites because of the neutralization of positive and negative charges inside TiO_2. This can effectively improve the charge transport efficiency and thus enhance the photocatalytic activity [342]. For example, the Mo–C co-doped TiO_2 powders prepared by thermal oxidation of a mixture of TiC and MoO_3 in the air have the potential of visible light harvesting (Fig. 15e) and effective photoexcited charge separation, and can thus exhibit higher photocatalytic activity when compared with anatase TiO_2 (Fig. 15f) [343].

The fabrication of semiconductor heterostructures is one of many effective methods developed in recent years to photoexcite and separate the electro-hole pairs. Compared to a single semiconductor, heterogeneous semiconductors are ideal for light-harvesting devices such as photovoltaic and photoelectrochemical

cells, because heterogeneous semiconductor electrodes are able to absorb a larger fraction of the solar spectrum and thus generate more photoinduced electron-hole pairs [344, 345]. Moreover, the coupling of two different semiconductors with proper conduction band potentials facilitates the transfer of electrons from an excited small band gap semiconductor into neighboring semiconductors. This facilitates charge separation and improves device performance.

Many metal oxides (such as Bi_2O_3 [346], Al_2O_3 [347], Cu_2O [348], Fe_2O_3 [349], MoO_3 [312], SnO_2 [350], SiO_2 [351], WO_3 [245], ZnO [352], and ZrO_2 [353]) and metal sulfides (such as Bi_2S_3 [346], Cu_2S [354], CdS [355], PbS [356], and Ag_2S [357]) have been reported to couple with TiO_2 to form heterostructured photocatalysts with enhanced photocatalytic performance. TiO_2 surface modification with an insulating layer, such as $SrCO_3$ [358], Al_2O_3 [359], La_2O_3 [302] and MgO [361], or a higher conduction band edge semiconductor layer, such as SnO_2 [362], In_2O_3 [314], Nb_2O_5 [226], and ZnO [363], was proven effective in reducing the recombination and increasing the DSSCs conversion efficiency. $Bi_4Ti_3O_{12}$/TiO_2 heterostructures composed of $Bi_4Ti_3O_{12}$ nanosheets on the surface of TiO_2 submicron fibers were prepared via a facile two-step synthesis route combining an electrospinning method and hydrothermal process. These heterostructures showed a higher degradation rate of rhodamine B (RhB) than the pure TiO_2 submicron fibers under visible light. This is largely due to the extended absorption in the visible light spectrum resulting from the $Bi_4Ti_3O_{12}$ nanosheets, and the effective separation of photoexcited charges driven by the photoinduced potential difference generated at the $Bi_4Ti_3O_{12}$/TiO_2 interface [364]. TiO_2 nanotube arrays sensitized with $ZnFe_2O_4$ nanocrystals (Fig. 16a) were successfully fabricated by a two-step process of anodization and vacuum-assisted impregnation followed by annealing. It has been shown that the $ZnFe_2O_4$ sensitization enhanced the photoinduced charge separation (Fig. 16b, c) and extended the range of the photoresponse of TiO_2 nanotube arrays from the UV to the visible region [365]. TiO_2-multiwalled carbon nanotube (MWCNT) nanocomposites (Fig. 16d) synthesized by hydrothermal processes possess a 50 % enhancement in the conversion efficiency (4.9–7.37 %) of DSSCs compared to hydrothermally synthesized TiO_2 without MWCNTs and Degussa P25. Efficient charge transfer in the nanocomposites is a possible reason for the enhancement (Fig. 16e, f) [366].

As the most recently discovered carbonaceous material, graphene has attracted extensive attention as a useful material for solar energy applications. With a unique sp^2 hybrid carbon network, a large theoretical specific surface area (2,630 m^2g^{-1}), a high thermal conductivity (5,000 $Wm^{-1}K^{-1}$), a large intrinsic electron mobility (200, 000 $cm^2V^{-1}s^{-1}$), and good mechanical stability, it has applications in sensors, catalysts, and energy conversion [223]. Graphene can serve as a strong electron collector and carrier in a TiO_2/graphene composite system because their energy levels and physical properties are compatible [367]. Graphene-TiO_2 composites are also highly desirable for their promising energy and environmental remediation applications.

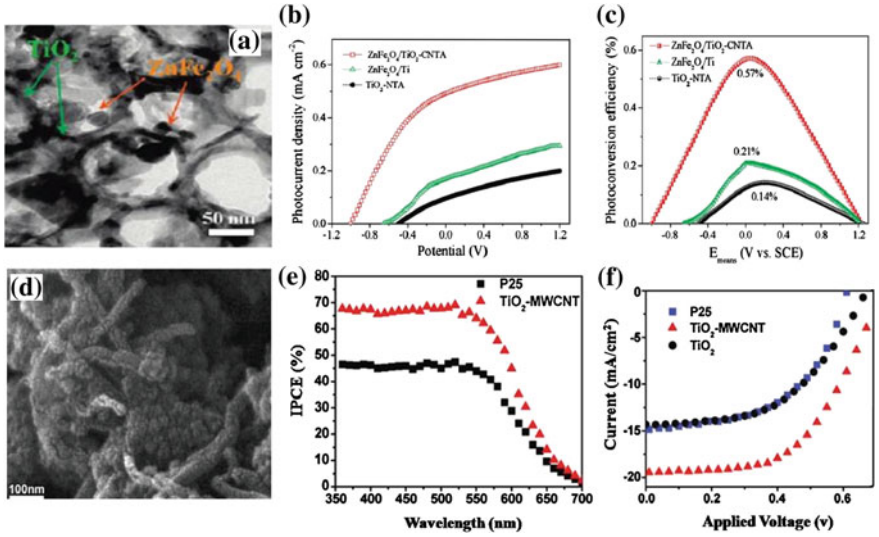

Fig. 16 SEM images of $ZnFe_2O_4/TiO_2$ nanotubes (**a**) and TiO_2 MWCNT nanocomposite (**d**). **b** Variation of the photocurrent density versus bias potential (versus SCE) and **c** Photoconversion efficiency as a function of the applied potential (versus SCE) based on (**a**). IPCE curves (**e**) and current–voltage characteristics (**f**) of DSSCs based on TiO_2 MWCNT nanocomposite (**c**). (Reprinted with permission from Ref. **a–c** [365], **d–f** [366]. Copyright © American Chemical Society)

Several synthetic strategies have been designed to fabricate graphene-TiO_2 photocatalysts. In the first method, well-defined TiO_2 structures are deposited on the surface of graphene oxide (GO) under vigorous stirring or ultrasonic agitation [368–370]. The site-specific oxygenated groups on GO favor a uniform distribution of TiO_2 across the surface. Graphene-TiO_2 photocatalysts are obtained after the reduction of GO in the composite [371, 372]. Yang et al. packed TiO_2 and graphene nanosheets into a 2D unit (TiO_2/graphene) that is structurally similar to a thylakoid in the chloroplast of photosynthetic plants. In this 2D unit, TiO_2 performs as a photo-electric conversion center to absorb light and excite the electrons, while graphene is like the cytochrome b6f complex capturing electrons and transporting them out of the circuit. Such a novel structure was formed by stacking TiO_2 nanosheets and GO nanosheets using a layer-by-layer (LBL) assembly technique in the presence of charged poly(diallyldimethylammonium chloride) (PDDA) which supplied the counter-ions. GO was reduced to graphene by hydrazine and annealed under argon flow at 400 °C and the PDDA was then removed by calcining at 450 °C in air. The graphene-TiO_2 stacking film can produce an anodic current 20 times larger than pure TiO_2 stacking films. Interestingly, the current further increased with thicker films [373]. Another significant example, graphene-wrapped anatase TiO_2 nanoparticles (Fig. 17a) with a significant reduction in the band gap (2.80 eV, Fig. 17b) were prepared by wrapping

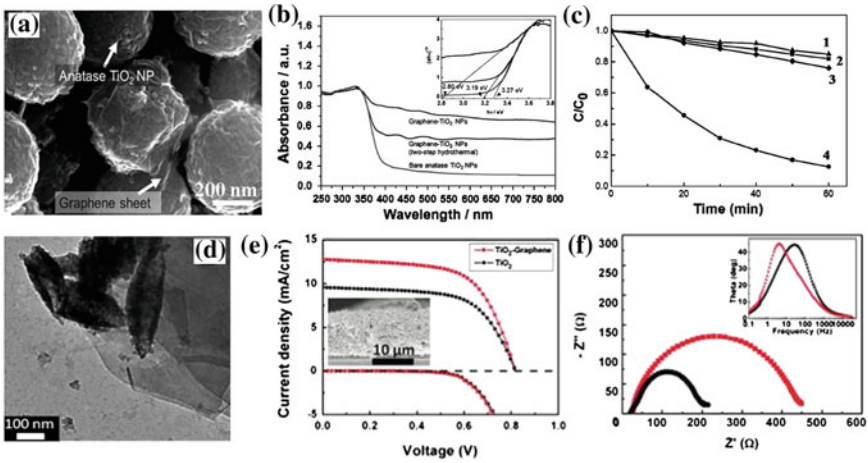

Fig. 17 **a** SEM image, **b** UV-visible spectra (the *inset* is the band gap (E_g) of samples estimated from the absorption edge), and **c** photodegradation of MB under visible light (1: P25, 2: bare anatase TiO_2 NPs, 3: graphene-TiO_2 NPs (two-step hydrothermal), 4: graphene-TiO_2 NPs). **d** TEM image of TiO_2-graphene composite, **e** current–voltage characteristic, and **f** Nyquist plots of DSSCs using TiO_2-graphene composite (the *inset* is the corresponding Bode plots in electrochemical impedance spectra (EIS) test). (Reprinted with permission from Ref. **a–c** [374], **d–f** [377]. Copyright © American Chemical Society and Wiley-VCH)

amorphous TiO_2 NPs with GO, followed by continuous GO reduction and TiO_2 crystallization via hydrothermal treatment. The graphene-TiO_2 nanoparticles possess excellent photocatalytic properties under visible light for the degradation of MB (Fig. 17c) [374].

In the second method, graphene-TiO_2 photocatalysts are fabricated by an in situ growth of TiO_2 on graphene sheets [375, 376]. By introducing cetyltrimethylammonium bromide (CTAB)-functionalized DMF-soluble graphene into the polymeric solution for electrospinning, graphene was successfully integrated into the TiO_2 rice-shaped nanostructures (Fig. 17d). The obtained composites displayed enhanced photovoltaic and photocatalytic properties compared to pure TiO_2 nanorices when used in DSSCs (Fig. 17e, f) and in the photocatalytic degradation of methyl orange (MO) [377]. In addition, a series of graphene-TiO_2 composites with different graphene contents can be controllably synthesized by a sol–gel method [378]. Graphene-TiO_2 composites demonstrated a higher photocatalytic activity compared to P25 with respect to hydrogen generation from water splitting. The highest photocatalytic activity was observed for the sample with 5 % graphene, suggesting that an excess of graphene will decrease the activity by introducing electron–hole recombination centers into the composite [378].

In the third method, TiO_2 structures are grown in situ onto GO followed by the reduction of GO in a subsequent reaction step using UV light or microwave irradiation [379, 380]. For example, novel hollow spheres consisting of $Ti_{0.91}O_2$ nanosheets and graphene nanosheets (Fig. 18a) were successfully fabricated by a

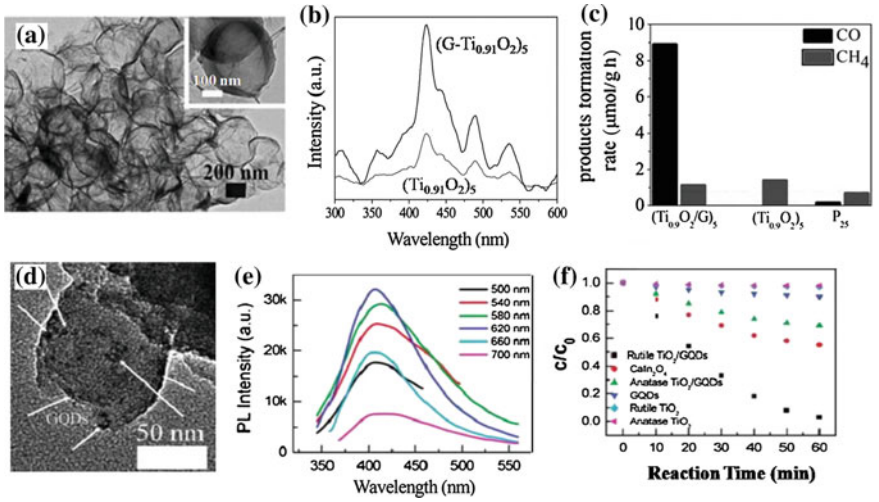

Fig. 18 TEM images of $(G\text{-}Ti_{0.91}O_2)_5$ hollow spheres (**a**) and rutile TiO_2/graphene quantum dot composites (**d**). **b** PL emission spectra of $(Ti_{0.91}O_2)_5$ hollow spheres and $(G\text{-}Ti_{0.91}O_2)_5$ hollow spheres (**a**). **c** Photocatalytic CH_4 and CO evolution rates for $(Ti_{0.91}O_2)_5$ hollow spheres $(G\text{-}Ti_{0.91}O_2)_5$ hollow spheres (**a**) and P25. **e** Upconverted PL spectra of the graphene quantum dots (**b**) at different excitation wavelengths and **f** photocatalytic degradation of MB under visible light irradiation using different catalysts. (Reprinted with permission from Ref. **a–c** [380], **d–f** [388]. Copyright © Wiley-VCH and American Chemical Society)

layer-by-layer assembly technique with polymer PMMA beads as sacrificial templates. Subsequently, microwave irradiation was used to simultaneously remove the template and reduce graphene oxide into graphene. The sufficiently compact stacking of ultrathin $Ti_{0.91}O_2$ nanosheets with graphene nanosheets facilitated the photogenerated electron to quickly transfer from the $Ti_{0.91}O_2$ nanosheets to graphene and enhance the lifetime of the charge carriers and improve photocatalytic activity (Fig. 18b, c) [380].

In the fourth method, the in situ growth of TiO_2 structures and reduction of GO are simultaneously accomplished through a simple one-pot growth method [381, 382]. This strategy is a particularly convenient procedure for the fabrication of graphene-TiO_2 photocatalysts. The reducing environment can be achieved by using either a reducing solvent or by directly adding a reducing agent [383, 384]. For example, exposed (001) facet TiO_2-graphene composite photocatalysts were successfully produced via a direct one-step hydrothermal method in an ethanol–water solvent. The resulting composite exhibited an extended visible light absorption range due to the formation of a chemical Ti–O–C bond and enhanced charge separation by virtue of the formation of nano-sized Schottky interfaces at the contacts between TiO_2 and graphene. This leads to significant improvement in photodegredation of MB (or MO) dye when compared to P25 films under both UV and visible light irradiation [367].

Recently, graphene quantum dots (GQDs) have become an active area of research. Compared to graphene with 2D nanosheets and 1D nanoribbon structures, 0D GQDs possess strong quantum confinement and edge effects when their sizes approach 10 nm or less. At this scale, new physical properties become apparent [385–387]. Zhuo et al. presented the synthesis of GQDs with excellent PL properties using a direct and simple ultrasonic reaction process. The composite photocatalysts (rutile TiO_2/GQD and anatase TiO_2/GQD systems) were prepared by mixing GQDs with TiO_2 nanoparticles (Fig. 18d) in order to harvest the visible spectrum of sunlight using the upconversion photoluminescence (PL) properties of GQDs (Fig. 18e). It was observed that the photocatalytic activity of the rutile TiO_2/GQD composite was superior to that of the anatase TiO_2/GQD composite under visible light ($\lambda > 420$ nm) irradiation in the degradation of MB (Fig. 18f) [388].

3 Conclusion

The challenge of effectively converting solar energy into useful energy will require more advanced materials. As one of the most promising functional materials for efficient, high performance, and cost-effective solar energy applications, TiO_2 nanostructures of various morphologies will continue to be an area of active research. It has been shown that every structure possesses its own advantages, such as large surface area for nanoparticle systems, effective charge separation, and transport for vertically ordered nanotubes or nanorods, a high percentage of reactive (001) facets for nanosheets, and efficient light scattering for 3D hierarchical structures, to name a few. Correspondingly, the different morphologies are derived from different characteristic synthesis methods. The sol–gel method, for example, is a simple and low-cost process to prepare nanoparticles. The hydrothermal method can be used to fabricate several structures (e.g., nanosheet, nanorod and hierarchical architecture), whereas the facile electrochemical anodization can lead to oriented nanotube arrays. Clearly, numerous strategies have been exploited to modify pure TiO_2, which suffers from the shortcomings of a narrow light absorption range (restricted to UV) and rapid charge recombination. With more efforts geared toward the fabrication of high-quality TiO_2-based nanomaterials and economically feasible synthesis procedures, there is little doubt that the future of solar energy technology and its practical applications will remain bright.

References

1. Liu J, Cao GZ, Yang ZG, Wang DH, Dubois D, Zhou XD, Graff GL, Pederson LR, Zhang JG (2008) ChemSusChem 1:676–697
2. Hagfeldt A, Boschloo G, Sun LC, Kloo L, Pettersson H (2010) Chem Rev 110:6595–6663
3. Kamat PV (2007) J Phys Chem C 111:2834–2860

4. Nozik A, Miller J (2010) Chem Rev 110:6443–6445
5. Liu C, Burghaus U, Besenbacher F, Wang ZL (2010) ACS Nano 4:5517–5526
6. Serrano E, Rus G, García-Martínez J (2009) Renew Sustain Energy Rev 13:2373–2384
7. Beard MC, Ellingson RJ (2008) Laser Photonics Rev 2:377–399
8. Bisquert J, Cahen D, Hodes G, Ruhle S, Zaban A (2004) J Phys Chem B 108:8106–8118
9. Gratzel M (2001) Nature 414:338–344
10. Green MA (2001) Prog Photovoltaics Res Appl 9:123–135
11. El Chaar L, El Zein N (2011) Renew Sustain Energy Rev 15:2165–2175
12. Lewis NS (2007) Science 315:798–801
13. Gratzel M (2006) Prog Photovoltaics Res Appl 14:429–442
14. Oregan B, Gratzel M (1991) Nature 353:737–740
15. Yella A, Lee H-W, Tsao HN, Yi C, Chandiran AK, Nazeeruddin MK, Diau EW-G, Yeh C-Y, Zakeeruddin SM, Grätzel M (2011) Science 334:629–634
16. Grätzel M (2003) J Photochem Photobiol C 4:145–153
17. Toivola M, Halme J, Miettunen K, Aitola K, Lund PD (2009) Int J Energy Res 33:1145–1160
18. Halme J, Vahermaa P, Miettunen K, Lund P (2010) Adv Mater 22:E210–E234
19. O'Regan BC, Durrant JR (2009) Acc Chem Res 42:1799–1808
20. Chen XB (2009) Chin J Catal 30:839–851
21. Galinska A, Walendziewski J (2005) Energy Fuels 19:1143–1147
22. Yang XH, Li Z, Liu G, Xing J, Sun C, Yang HG, Li C (2010) CrystEngComm 13:1378–1383
23. Chen XB, Shen SH, Guo LJ, Mao SS (2010) Chem Rev 110:6503–6570
24. Fujishima A, Honda K (1972) Nature 238:37
25. Ni M, Leung MKH, Leung DYC, Sumathy K (2007) Renew Sustain Energy Rev 11:401–425
26. Zhang QJ, Sun CH, Yan J, Hu XJ, Zhou SY, Chen P (2010) Solid State Sci 12:1274–1277
27. Lee JS (2005) Catal Surv Asia 9:217–227
28. Walter MG, Warren EL, McKone JR, Boettcher SW, Mi Q, Santori EA, Lewis NS (2010) Chem Rev 110:6446
29. Ye M, Vennerberga D, Lin C, Lin Z (2012) J Nanosci Lett 2:1
30. Youngblood WJ, Lee SHA, Maeda K, Mallouk TE (2009) Acc Chem Res 42:1966–1973
31. Kaur A, Gupta U (2009) J Mater Chem 19:8279–8289
32. Akpan UG, Hameed BH (2009) J Hazard Mater 170:520–529
33. Pelaez M, Nolan NT, Pillai SC, Seery MK, Falaras P, Kontos AG, Dunlop PSM, Hamilton JWJ, Byrne JA, O'shea K (2012) Appl Catal B 125:331–349
34. Hu X, Li G, Yu JC (2009) Langmuir 26:3031–3039
35. Chen X, Mao SS (2007) Chem Rev 107:2891–2959
36. Lv M, Zheng D, Ye M, Sun L, Xiao J, Guo W, Lin C (2012) Nanoscale 4:5872–5879
37. Chou TP, Zhang QF, Russo B, Fryxell GE, Cao GZ (2007) J Phys Chem C 111:6296–6302
38. Mor GK, Varghese OK, Paulose M, Shankar K, Grimes CA (2006) Sol Energy Mater Sol Cells 90:2011–2075
39. Shankar K, Basham JI, Allam NK, Varghese OK, Mor GK, Feng XJ, Paulose M, Seabold JA, Choi KS, Grimes CA (2009) J Phys Chem C 113:6327–6359
40. Fei H, Yang Y, Rogow DL, Fan X, Oliver SRJ (2010) ACS Appl Mater Interfaces 2:974–979
41. Nozik AJ (2010) Nano Lett 10:2735–2741
42. Arico AS, Bruce P, Scrosati B, Tarascon JM, Van Schalkwijk W (2005) Nat Mater 4:366–377
43. Guo YG, Hu JS, Wan LJ (2008) Adv Mater 20:2878–2887
44. Xin X, He M, Han W, Jung J, Lin Z (2011) Angew Chem Int Ed 50:11739–11742
45. Choi SK, Kim S, Lim SK, Park H (2010) J Phys Chem C 114:16475–16480
46. Xin X, Wang J, Han W, Ye M, Lin Z (2012) Nanoscale 4:964–969
47. Xin X, Scheiner M, Ye M, Lin Z (2011) Langmuir 27:14594–14598
48. Hartmann P, Lee DK, Smarsly BM, Janek J (2010) ACS Nano 4:3147–3154

49. Alivov Y, Fan ZY (2009) J Phys Chem C 113:12954–12957
50. Li Y, Fang XS, Koshizaki N, Sasaki T, Li L, Gao SY, Shimizu Y, Bando Y, Golberg D (2009) Adv Funct Mater 19:2467–2473
51. Kumar A, Madaria AR, Zhou CW (2010) J Phys Chem C 114:7787–7792
52. Albu SP, Roy P, Virtanen S, Schmuki P (2010) Isr J Chem 50:453–467
53. Yu JG, Fan JJ, Lv KL (2010) Nanoscale 2:2144–2149
54. Bleta R, Alphonse P, Lorenzato L (2010) J Phys Chem C 114:2039–2048
55. Isley SL, Penn RL (2008) J Phys Chem C 112:4469–4474
56. Liu JJ, Qin W, Zuo SL, Yu YC, Hao ZP (2009) J Hazard Mater 163:273–278
57. Wang J, Lin ZQ (2009) J Phys Chem C 113:4026–4030
58. Zhang W, Zhu R, Ke L, Liu XZ, Liu B, Ramakrishna S (2010) Small 6:2176–2182
59. Hwang D, Lee H, Jang SY, Jo SM, Kim D, Seo Y, Kim DY (2011) ACS Appl Mater Interfaces 3:2719–2725
60. Wu MS, Tsai CH, Wei TC (2011) Chem Commun 47:2871–2873
61. Bala H, Jiang L, Fu WY, Yuan GY, Wang XD, Liu ZR (2010) Appl Phys Lett 97:153108
62. Suprabha T, Roy HG, Thomas J, Kumar KP, Mathew S (2009) Nanoscale Res Lett 4:144–152
63. Melhem H, Simon P, Beouch L, Goubard F, Boucharef M, Di Bin C, Leconte Y, Ratier B, Herlin-Boime N, Bouclon J (2011) Adv Energy Mater 1:908–916
64. Pradhan SK, Reucroft PJ (2003) J Cryst Growth 250:588–594
65. Yu DH, Yu X, Wang C, Liu XC, Xing Y (2012) ACS Appl Mater Interfaces 4:2781–2787
66. Koo B, Park J, Kim Y, Choi SH, Sung YE, Hyeon T (2006) J Phys Chem B 110:24318–24323
67. Ahn SH, Chi WS, Park JT, Koh JK, Roh DK, Kim JH (2012) Adv Mater 24:519–522
68. Guldin S, Huttner S, Kolle M, Welland ME, Muller-Buschbaum P, Friend RH, Steiner U, Tétreault N (2010) Nano Lett 10:2303–2309
69. Halaoui LI, Abrams NM, Mallouk TE (2005) J Phys Chem B 109:6334–6342
70. Ismagilov ZR, Tsikoza LT, Shikina NV, Zarytova VF, Zinoviev VV, Zagrebelnyi SN (2009) Russ Chem Rev 78:873–885
71. Han S, Choi SH, Kim SS, Cho M, Jang B, Kim DY, Yoon J, Hyeon T (2005) Small 1:812–816
72. Jin WM, Shin JH, Cho CY, Kang JH, Park JH, Moon JH (2010) ACS Appl Mater Interfaces 2:2970–2973
73. Hatton B, Mishchenko L, Davis S, Sandhage KH, Aizenberg J (2010) PNAS 107:10354–10359
74. Shopsowitz KE, Stahl A, Hamad WY, MacLachlan MJ (2012) Angew Chem Int Ed 51:6886–6890
75. Ahn SH, Park JT, Koh JK, Roh DK, Kim JH (2011) Chem Commun 47:5882–5884
76. Agarwala S, Kevin M, Wong A, Peh C, Thavasi V, Ho G (2010) ACS Appl Mater Interfaces 2:1844–1850
77. Ismail AA, Bahnemann DW (2011) J Mater Chem 21:11686–11707
78. Park JT, Chi WS, Roh DK, Ahn SH, Kim JH (2012) Adv Funct Mater 23:26–33
79. Kim YJ, Lee YH, Lee MH, Kim HJ, Pan JH, Lim GI, Choi YS, Kim K, Park NG, Lee C (2008) Langmuir 24:13225–13230
80. Yang SC, Yang DJ, Kim J, Hong JM, Kim HG, Kim ID, Lee H (2008) Adv Mater 20:1059–1064
81. Mandlmeier B, Szeifert JM, Fattakhova-Rohlfing D, Amenitsch H, Bein T (2011) J Am Chem Soc 133:17274–17282
82. Xiong Z, Dou H, Pan J, Ma J, Xu C, Zhao X (2010) CrystEngComm 12:3455–3457
83. Sjöström T, McNamara LE, Yang L, Dalby M, Su B (2012) ACS Appl Mater Interfaces 4:6354–6361
84. Jang YH, Xin X, Byun M, Jang YJ, Lin Z, Kim DH (2011) Nano Lett 12:479–485
85. Hayward RC, Chmelka BF, Kramer EJ (2005) Adv Mater 17:2591–2595

86. Zhao D, Feng D, Luo W, Zhang J, Xu M, Zhang R, Wu H, Lv Y, Asiri AM, Rahman M (2013) J Mater Chem A 1:1591–1599
87. Cha MA, Shin C, Kannaiyan D, Jang YH, Kochuveedu ST, Kim DH (2009) J Mater Chem 19:7245–7250
88. Guldin S, Docampo P, Stefik M, Kamita G, Wiesner U, Snaith HJ, Steiner U (2012) Small 3:432–440
89. Chen Y, Kim HC, McVittie J, Ting C, Nishi Y (2010) Nanotechnology 21:185303
90. Ahmed S, Du Pasquier A, Birnie DP III, Asefa T (2011) ACS Appl Mater Interfaces 3:3002–3010
91. Dutta S, Patra AK, De S, Bhaumik A, Saha B (2012) ACS Appl Mater Interfaces 4:1560–1564
92. Kwak ES, Lee W, Park NG, Kim J, Lee H (2009) Adv Funct Mater 19:1093–1099
93. Mihi A, Zhang C, Braun PV (2011) Angew Chem Int Ed 123:5830–5833
94. Campbell M, Sharp D, Harrison M, Denning R, Turberfield A (2000) Nature 404:53–56
95. Nishimura S, Abrams N, Lewis BA, Halaoui LI, Mallouk TE, Benkstein KD, van de Lagemaat J, Frank AJ (2003) J Am Chem Soc 125:6306–6310
96. Lee SHA, Abrams NM, Hoertz PG, Barber GD, Halaoui LI, Mallouk TE (2008) J Phys Chem B 112:14415–14421
97. Shin JH, Moon JH (2011) Langmuir 27:6311–6315
98. Chang SY, Chen SF, Huang YC (2011) J Phys Chem C 115:1600–1607
99. Cho CY, Moon JH (2011) Adv Mater 23:2971–2975
100. Berrigan JD, McLachlan TM, Deneault JR, Cai Y, Kang TS, Durstock MF, Sandhage K (2013) J Mater Chem A 1:128–134
101. Xu C, Shin PH, Cao L, Wu J, Gao D (2009) Chem Mater 22:143–148
102. Shao W, Gu F, Gai L, Li C (2011) Chem Commun 47:5046–5048
103. Joo JB, Zhang Q, Lee I, Dahl M, Zaera F, Yin Y (2012) Adv Funct Mater 22:166–174
104. Thompson GE (1997) Thin Solid Films 297:192–201
105. Koh JH, Koh JK, Seo JA, Shin JS, Kim JH (2011) Nanotechnology 22:365401
106. Wang H (2012) CrystEngComm 14:6215–6220
107. Bian Z, Zhu J, Cao F, Huo Y, Lu Y, Li H (2010) Chem Commun 46:8451–8453
108. Tétreault N, Arsenault E, Heiniger LP, Soheilnia N, Brillet J, Moehl T, Zakeeruddin S, Ozin GA, Grätzel M (2011) Nano Lett 11:4579–4584
109. Liu L, Karuturi SK, Su LT, Tok AIY (2010) Energy Environ Sci 4:209–215
110. Tan LK, Liu X, Gao H (2011) J Mater Chem 21:11084–11087
111. Li L, Liu C (2009) J Phys Chem C 114:1444–1450
112. Yang W, Li J, Wang Y, Zhu F, Shi W, Wan F, Xu D (2011) Chem Commun 47:1809–1811
113. Yang H, Fang W, Yang X, Zhu H, Li Z, Zhao H, Yao X (2012) J Mater Chem 22:22082–22089
114. Wu B, Guo C, Zheng N, Xie Z, Stucky GD (2008) J Am Chem Soc 130:17563–17567
115. Yu J, Xiang Q, Ran J, Mann S (2010) CrystEngComm 12:872–879
116. Wang J, Bian Z, Zhu J, Li H (2013) J Mater Chem A 1:1296–1302
117. Jun Y, Casula MF, Sim JH, Kim SY, Cheon J, Alivisatos AP (2003) J Am Chem Soc 125:15981–15985
118. Wu D, Gao Z, Xu F, Chang J, Jiang K (2012) CrystEngComm 15:516–523
119. Nian JN, Teng HS (2006) J Phys Chem B 110:4193–4198
120. Horvath E, Kukovecz A, Konya Z, Kiricsi I (2007) Chem Mater 19:927–931
121. Guo WX, Xu C, Wang X, Wang SH, Pan CF, Lin CJ, Wang ZL (2012) J Am Chem Soc 134:4437–4441
122. Liu B, Aydil ES (2009) J Am Chem Soc 131:3985–3990
123. Chen D, Huang F, Cheng YB, Caruso RA (2009) Adv Mater 21:2206–2210
124. Liu M, Piao L, Lu W, Ju S, Zhao L, Zhou C, Li H, Wang W (2010) Nanoscale 2:1115–1117
125. Ye M, Liu HY, Lin C, Lin Z (2012) Small 9:312–321
126. Zhang D, Li G, Yang X, Jimmy CY (2009) Chem Commun 4381–4383

127. Zheng Z, Huang B, Qin X, Zhang X, Dai Y, Jiang M, Wang P, Whangbo MH (2009) Chem Eur J 15:12576–12579
128. Diebold U (2003) Surf Sci Rep 48:53–229
129. Gong XQ, Selloni A (2005) J Phys Chem B 109:19560–19562
130. Yang HG, Sun CH, Qiao SZ, Zou J, Liu G, Smith SC, Cheng HM, Lu GQ (2008) Nature 453:638–641
131. Gu L, Wang J, Cheng H, Du Y, Han X (2012) Chem Commun 48:6978–6980
132. He Z, Cai Q, Hong F, Jiang Z, Chen J, Song S (2012) Ind Eng Chem Res 51:5662–5668
133. Xiang Q, Yu J, Jaroniec M (2011) Chem Commun 47:4532–4534
134. Zheng Z, Huang B, Qin X, Zhang X, Dai Y, Jiang M, Wang P, Whangbo MH (2009) Chem Eur J 15:12576–12579
135. Zhang H, Han Y, Liu X, Liu P, Yu H, Zhang S, Yao X, Zhao H (2010) Chem Commun 46:8395–8397
136. Liu M, Piao L, Zhao L, Ju S, Yan Z, He T, Zhou C, Wang W (2010) Chem Commun 46:1664–1666
137. Li J, Cao K, Li Q, Xu D (2012) CrystEngComm 14:83–85
138. Li J, Xu D (2010) Chem Commun 46:2301–2303
139. Ma XY, Chen ZG, Hartono SB, Jiang HB, Zou J, Qiao SZ, Yang HG (2010) Chem Commun 46:6608–6610
140. Yu H, Tian B, Zhang J (2011) Chem Eur J 17:5499–5502
141. Kumar EN, Jose R, Archana P, Vijila C, Yusoff M, Ramakrishna S (2012) Energy Environ Sci 5:5401–5407
142. Liu B, Miao J (2012) RSC Adv 3:1222–1226
143. Dai Y, Cobley CM, Zeng J, Sun Y, Xia Y (2009) Nano Lett 9:2455–2459
144. Amano F, Prieto-Mahaney OO, Terada Y, Yasumoto T, Shibayama T, Ohtani B (2009) Chem Mater 21:2601–2603
145. Jung MH, Chu MJ, Kang MG (2012) Chem Commun 48:5016–5018
146. Xie S, Han X, Kuang Q, Fu J, Zhang L, Xie Z, Zheng L (2011) Chem Commun 47:6722–6724
147. Pan J, Wu X, Wang L, Liu G, Lu GQM, Cheng HM (2011) Chem Commun 47:8361–8363
148. Wang L, Zang L, Zhao J, Wang C (2012) Chem Commun 48:11736–11738
149. Li F, Xu J, Chen L, Ni B, Li X, Fu Z, Lu Y (2013) J Mater Chem A 1:225–228
150. Berger S, Hahn R, Roy P, Schmuki P (2010) Phys Status Solidi B 247:2424–2435
151. Peng XS, Wang JP, Thomas DF, Chen AC (2005) Nanotechnology 16:2389–2395
152. Gong D, Grimes CA, Varghese OK, Hu WC, Singh RS, Chen Z, Dickey EC (2001) J Mater Res 16:3331–3334
153. Wu XJ, Zhu F, Mu C, Liang YQ, Xu LF, Chen QW, Chen RZ, Xu DS (2010) Coord Chem Rev 254:1135–1150
154. Peter LM, Jennings JR, Ghicov A, Schmuki P, Walker AB (2008) J Am Chem Soc 130:13364–13372
155. Xiao P, Zhang YH, Garcia BB, Sepehri S, Liu DW, Cao GZ (2009) J Nanosci Nanotechnol 9:2426–2436
156. Allam NK, El-Sayed MA (2010) J Phys Chem C 114:12024–12029
157. Lai Y, Sun L, Chen Y, Zhuang H, Lin C (2006) J Electrochem Soc 153:D123–D127
158. Gong JJ, Lai YK, Lin CJ (2010) Electrochim Acta 55:4776–4782
159. Gong JJ, Lin CJ, Ye MD, Lai YK (2011) Chem Commun 47:2598–2600
160. Guo WX, Xue XY, Wang SH, Lin CJ, Wang ZL (2012) Nano Lett 12:2520–2523
161. Rattanavoravipa T, Sagawa T, Yoshikawa S (2008) Sol Energy Mater Sol Cells 92:1445–1449
162. Wender H, Feil AF, Diaz LB, Ribeiro CS, Machado GJ, Migowski P, Weibel DE, Dupont J, Teixeira SR (2011) ACS Appl Mater Interfaces 3:1359–1365
163. Tan YF, Yang L, Chen JZ, Qiu Z (2010) Langmuir 26:10111–10114
164. Alivov Y, Pandikunta M, Nikishin S, Fan ZY (2009) Nanotechnology 20:225602
165. Bao NZ, Yoriya S, Grimes CA (2011) J Mater Chem 21:13909–13912

166. Wang J, Zhao L, Lin VSY, Lin ZQ (2009) J Mater Chem 19:3682–3687
167. Wang J, Lin Z (2012) Chem Asian J 7:2754–2762
168. Su ZX, Zhou WZ (2011) J Mater Chem 21:8955–8970
169. Roy P, Kim D, Lee K, Spiecker E, Schmuki P (2010) Nanoscale 2:45–59
170. Roy P, Berger S, Schmuki P (2011) Angew Chem Int Ed 50:2904–2939
171. Nah YC, Paramasivam I, Schmuki P (2010) ChemPhysChem 11:2698–2713
172. Schmuki P, Macak JM, Tsuchiya H, Taveira L, Aldabergerova S (2005) Angew Chem Int Ed 44:7463–7465
173. Grimes CA, Allam NK, Shankar K (2008) J Mater Chem 18:2341–2348
174. Schmuki P, Kim D, Ghicov A, Albu SP (2008) J Am Chem Soc 130:16454
175. Fei GT, Jin Z, Hu XY, Xu SH, De Zhang L (2009) Chem Lett 38:288–289
176. Lin J, Liu K, Chen XF (2011) Small 7:1784–1789
177. Xu XJ, Tang CC, Zeng HB, Zhai TY, Zhang SQ, Zhao HJ, Bando Y, Golberg D (2011) ACS Appl Mater Interfaces 3:1352–1358
178. Schmuki P, Albu SP, Ghicov A, Aldabergenova S, Drechsel P, LeClere D, Thompson GE, Macak JM (2008) Adv Mater 20:4135
179. Li SQ, Zhang GM, Guo DZ, Yu LG, Zhang W (2009) J Phys Chem C 113:12759–12765
180. Stergiopoulos T, Ghicov A, Likodimos V, Tsoukleris DS, Kunze J, Schmuki P, Falaras P (2008) Nanotechnology 19:235602
181. Sun Y, Yan KP, Wang GX, Guo W, Ma TL (2011) J Phys Chem C 115:12844–12849
182. Biswas S, Shahjahan M, Hossain MF, Takahashi T (2010) Electrochem Commun 12:668–671
183. Chen CH, Chen KC, He JL (2010) Curr Appl Phys 10:S176–S179
184. Stergiopoulos T, Valota A, Likodimos V, Speliotis T, Niarchos D, Skeldon P, Thompson GE, Falaras P (2009) Nanotechnology 20:365601
185. Tang YX, Tao J, Tao HJ, Wu T, Wang L, Zhang YY, Li ZL, Tian XL (2008) Acta Phys Chim Sin 24:1120–1126
186. Leenheer AJ, Miedaner A, Curtis CJ, van Hest M, Ginley DS (2007) J Mater Res 22:681–687
187. Mor GK, Varghese OK, Paulose M, Grimes CA (2005) Adv Funct Mater 15:1291–1296
188. Varghese OK, Paulose M, Grimes CA (2009) Nat Nanotechnol 4:592–597
189. Sadek AZ, Zheng HD, Latham K, Wlodarski W, Kalantar-Zadeh K (2009) Langmuir 25:509–514
190. Wang DA, Yu B, Wang CW, Zhou F, Liu WM (2009) Adv Mater 21:1964–1967
191. Zhang G, Huang H, Zhang Y, Chan HLW, Zhou L (2007) Electrochem Commun 9:2854–2858
192. S. H. Kang, H. S. Kim, J. Y. Kim and Y. E. Sung, Nanotechnology, 2009, 20
193. Lei BX, Liao JY, Zhang R, Wang J, Su CY, Kuang DB (2010) J Phys Chem C 114:15228–15233
194. Lin J, Chen JF, Chen XF (2010) Electrochem Commun 12:1062–1065
195. Wang J, Lin ZQ (2008) Chem Mater 20:1257–1261
196. Ali G, Yoo SH, Kum JM, Kim YN, Cho SO (2011) Nanotechnology 22:245602
197. Wang J, Lin ZQ (2010) Chem Mater 22:579–584
198. Wang DA, Liu LF (2010) Chem Mater 22:6656–6664
199. Pang Q, Leng LM, Zhao LJ, Zhou LY, Liang CJ, Lan YW (2011) Mater Chem Phys 125:612–616
200. Wang DA, Liu LF, Zhang FX, Tao K, Pippel E, Domen K (2011) Nano Lett 11:3649–3655
201. Wang J, Lin ZQ (2008) Chem Mater 20:1257–1261
202. Lin CJ, Yu WY, Chien SH (2010) J Mater Chem 20:1073–1077
203. Wang YH, Yang HX, Liu Y, Wang H, Shen H, Yan J, Xu HM (2010) Prog Photovoltaics 18:285–290
204. Wang YH, Yang HX, Lu L (2010) J Appl Phys 108:064510
205. Liu ZY, Misra M (2010) ACS Nano 4:2196–2200
206. Zou DC, Wang D, Chu ZZ, Lv ZB, Fan X (2010) Coord Chem Rev 254:1169–1178

207. Liu Y, Wang H, Li M, Hong RJ, Ye QH, Zheng JM, Shen H (2009) Appl Phys Lett 95:233505
208. Liu Y, Li M, Wang H, Zheng JM, Xu HM, Ye QH, Shen H (2010) J Phys D Appl Phys 43:205103
209. Mor GK, Shankar K, Paulose M, Varghese OK, Grimes CA (2006) Nano Lett 6:215–218
210. Hu A, Li H, Jia Z, Xia Z (2011) J Solid State Chem 184:2936–2940
211. Hu A, Xiao L, Dai G, Xia Z (2012) J Solid State Chem 190:130–134
212. Ye MD, Xin XK, Lin CJ, Lin ZQ (2011) Nano Lett 11:3214–3220
213. Chen CC, Chung HW, Chen CH, Lu HP, Lan CM, Chen SF, Luo L, Hung CS, Diau EWG (2008) J Phys Chem C 112:19151–19157
214. Shang M, Wang W, Yin W, Ren J, Sun S, Zhang L (2010) Chem Eur J 16:11412–11419
215. Ding B, Kim H, Kim C, Khil M, Park S (2003) Nanotechnology 14:532
216. Li D, Wang Y, Xia Y (2003) Nano Lett 3:1167–1171
217. Reneker DH, Chun I (1999) Nanotechnology 7:216
218. Song MY, Ihn KJ, Jo SM, Kim DY (1861) Nanotechnology 2004:15
219. Huang ZM, Zhang YZ, Kotaki M, Ramakrishna S (2003) Compos Sci Technol 63:2223–2253
220. Choi SW, Park JY, Kim SS (2009) Nanotechnology 20:465603
221. Li D, Xia Y (2003) Nano Lett 3:555–560
222. Nair AS, Zhu P, Jagadeesh Babu V, Yang S, Krishnamoorthy T, Murugan R, Peng S, Ramakrishna S (2012) Langmuir 28:6202–6206
223. Wu MC, Sápi A, Avila A, Szabó M, Hiltunen J, Huuhtanen M, Tóth G, Kukovecz Á, Kónya Z, Keiski R (2011) Nano Research 4:360–369
224. Kumar A, Jose R, Fujihara K, Wang J, Ramakrishna S (2007) Chem Mater 19:6536–6542
225. Yang L, Leung WWF (2011) Adv Mater 23:4559–4562
226. Hwang SH, Kim C, Song H, Son S, Jang J (2012) ACS Appl Mater Interfaces 4:5287–5292
227. Jose R, Kumar A, Thavasi V, Ramakrishna S (2008) Nanotechnology 19:424004
228. Zhu P, Nair AS, Yang S, Peng S, Ramakrishna S (2011) J Mater Chem 21:12210–12212
229. Zhan S, Chen D, Jiao X, Tao C (2006) J Phys Chem B 110:11199–11204
230. Lee BH, Song MY, Jang SY, Jo SM, Kwak SY, Kim DY (2009) J Phys Chem C 113:21453–21457
231. Nair AS, Shengyuan Y, Peining Z, Ramakrishna S (2010) Chem Commun 46:7421–7423
232. Shengyuan Y, Peining Z, Nair AS, Ramakrishna S (2011) J Mater Chem 21:6541–6548
233. Hwang D, Jo SM, Kim DY, Armel V, MacFarlane DR, Jang SY (2011) ACS Appl Mater Interfaces 3:1521–1527
234. Ishida M, Park SW, Hwang D, Koo YB, Sessler JL, Kim DY, Kim D (2011) J Phys Chem C 115:19343–19354
235. Chen X, Liu L, Peter YY, Mao SS (2011) Science 331:746–750
236. An HL, Ahn HJ (2012) Mater Lett 81:41–44
237. Fujihara K, Kumar A, Jose R, Ramakrishna S, Uchida S (2007) Nanotechnology 18:365709
238. Liu B, Nakata K, Sakai M, Saito H, Ochiai T, Murakami T, Takagi K, Fujishima A (2012) Catal Sci Technol 2:1933–1939
239. Hwang D, Lee H, Seo Y, Kim D, Jo SM, Kim DY (2013) J Mater Chem A 1:1359–1367
240. Lee H, Hwang D, Jo SM, Kim D, Seo Y, Kim DY (2012) ACS Appl Mater Interfaces 4:3308–3315
241. Jang SY, Hwang D, Kim DY, Kim D (2013) J Mater Chem A 1:1228–1238
242. Yang HY, Lee MF, Huang CH, Lo YS, Chen YJ, Wong MS (2009) Thin Solid Films 518:1590–1594
243. Wolcott A, Smith WA, Kuykendall TR, Zhao Y, Zhang JZ (2008) Small 5:104–111
244. Larsen GK, Fitzmorris R, Zhang JZ, Zhao Y (2011) J Phys Chem C 115:16892–16903
245. Smith W, Wolcott A, Fitzmorris RC, Zhang JZ, Zhao Y (2011) J Mater Chem 21:10792–10800
246. Wang S, Xia G, He H, Yi K, Shao J, Fan Z (2007) J Alloy Compd 431:287–291

247. Pihosh Y, Turkevych I, Ye J, Goto M, Kasahara A, Kondo M, Tosa M (2009) J Electrochem Soc 156:K160–K165
248. Gamez F, Plaza-Reyes A, Hurtado P, Guillen F, Anta JA, Martinez-Haya B, Perez S, Sanz M, Castillejo M, Izquierdo JG, Banares L (2010) J Phys Chem C 114:17409–17415
249. Sanz M, Walczak M, de Nalda R, Oujja M, Marco JF, Rodriguez J, Izquierdo JG, Banares L, Castillejo M (2009) Appl Surf Sci 255:5206–5210
250. Sanz M, Walczak M, Oujja M, Cuesta A, Castillejo M (2009) Thin Solid Films 517:6546–6552
251. Yang XF, Zhuang JL, Li XY, Chen DH, Ouyang GF, Mao ZQ, Han YX, He ZH, Liang CL, Wu MM, Yu JC (2009) ACS Nano 3:1212–1218
252. Quinonez C, Vallejo W, Gordillo G (2010) Appl Surf Sci 256:4065–4071
253. Shan AY, Ghazi TIM, Rashid SA (2010) Appl Catal A 389:1–8
254. Seifried S, Winterer M, Hahn H (2000) Chem Vap Deposition 6:239–244
255. Zhang C, Chen S, Mo L, Huang Y, Tian H, Hu L, Huo Z, Dai S, Kong F, Pan X (2011) J Phys Chem C 115:16418–16424
256. Xu L, Steinmiller EMP, Skrabalak SE (2011) J Phys Chem C 116:871–877
257. Yu H, Irie H, Shimodaira Y, Hosogi Y, Kuroda Y, Miyauchi M, Hashimoto K (2010) J Phys Chem C 114:16481–16487
258. Zhu J, Ren J, Huo Y, Bian Z, Li H (2007) J Phys Chem C 111:18965–18969
259. Wu Q, Ouyang JJ, Xiea KP, Sun L, Wang MY, Lin CJ (2012) J Hazard Mater 199:410–417
260. Di Paola A, Marci G, Palmisano L, Schiavello M, Uosaki K, Ikeda S, Ohtani B (2002) J Phys Chem B 106:637–645
261. Huang JH, Hung PY, Hu SF, Liu RS (2010) J Mater Chem 20:6505–6511
262. Liqiang J, Xiaojun S, Baifu X, Baiqi W, Weimin C, Honggang F (2004) J Solid State Chem 177:3375–3382
263. Liu Z, Li Y, Liu C, Ya J (2011) L. E., W. Zhao, D. Zhao and L. An. ACS Appl Mater Interfaces 3:1721–1725
264. Wang E, Yang W, Cao Y (2009) J Phys Chem C 113:20912–20917
265. Li H, Zhang X, Huo Y, Zhu J (2007) Environ Sci Technol 41:4410–4414
266. Wu G, Nishikawa T, Ohtani B, Chen A (2007) Chem Mater 19:4530–4537
267. Song J, Yang HB, Wang X, Khoo SY, Wong C, Liu XW, Li CM (2012) ACS Appl Mater Interfaces 4:3712–3717
268. Liu G, Yin LC, Wang J, Niu P, Zhen C, Xie Y, Cheng HM (2012) Energy Environ Sci 5:9603–9610
269. Zhao Y, Qiu X, Burda C (2008) Chem Mater 20:2629–2636
270. Peng T, Dai K, Yi H, Ke D, Cai P, Zan L (2008) Chem Phys Lett 460:216–219
271. Liao G, Chen S, Quan X, Chen H, Zhang Y (2010) Environ Sci Technol 44:3481–3485
272. Park J, Yi J, Tachikawa T, Majima T, Choi W (2010) J Phys Chem Lett 1:1351–1355
273. Park H, Choi W (2005) J Phys Chem B 109:11667–11674
274. Zhang H, Zong R, Zhao J, Zhu Y (2008) Environ Sci Technol 42:3803–3807
275. Zhou X, Peng F, Wang H, Yu H, Fang Y (2011) Chem Commun 47:10323–10325
276. Zhang M, Shao C, Guo Z, Zhang Z, Mu J, Cao T, Liu Y (2011) ACS Appl Mater Interfaces 3:369–377
277. Wang H, Bai Y, Zhang H, Zhang Z, Li J, Guo L (2010) J Phys Chem C 114:16451–16455
278. Zhu G, Pan L, Xu T, Sun Z (2011) ACS Appl Mater Interfaces 3:1472–1478
279. Wang CL, Sun L, Yun H, Li J, Lai YK, Lin CJ (2009) Nanotechnology 20:295601
280. Hou Y, Li X, Zou X, Quan X, Chen G (2008) Environ Sci Technol 43:858–863
281. Zhou W, Liu H, Wang J, Liu D, Du G, Cui J (2010) ACS Appl Mater Interfaces 2:2385–2392
282. Kim JY, Choi SB, Noh JH, Yoon SH, Lee S, Noh TH, Frank AJ, Hong KS (2009) Langmuir 25:5348–5351
283. Huang H, Li D, Lin Q, Shao Y, Chen W, Hu Y, Chen Y, Fu X (2009) J Phys Chem C 113:14264–14269
284. Murakami N, Kurihara Y, Tsubota T, Ohno T (2009) J Phys Chem C 113:3062–3069

285. Zhang X, Zhang L, Xie T, Wang D (2009) J Phys Chem C 113:7371–7378
286. Colón G, López SM, Hidalgo M, Navío J (2010) Chem Commun 46:4809–4811
287. Gao XF, Li HB, Sun WT, Chen Q, Tang FQ, Peng LM (2009) J Phys Chem C 113:7531–7535
288. Lee HJ, Leventis HC, Moon SJ, Chen P, Ito S, Haque SA, Torres T, Nüesch F, Geiger T, Zakeeruddin SM (2009) Adv Funct Mater 19:2735–2742
289. O'Hayre R, Nanu M, Schoonman J, Goossens A, Wang Q, Grätzel M (2006) Adv Funct Mater 16:1566–1576
290. Wang Y, Gong H, Fan B, Hu G (2010) J Phys Chem C 114:3256–3259
291. Zhang Z, Shao C, Li X, Sun Y, Zhang M, Mu J, Zhang P, Guo Z, Liu Y (2012) Nanoscale 5:606–618
292. Pandikumar A, Murugesan S, Ramaraj R (2010) ACS Appl Mater Interfaces 2:1912–1917
293. Z. Bian, J. Zhu, F. Cao, Y. Lu and H. Li, Chem. Commun., 2009, 3789-3791
294. Seh ZW, Liu S, Low M, Zhang SY, Liu Z, Mlayah A, Han MY (2012) Adv Mater 24:2310–2314
295. Lee SS, Oh K (2012) ACS Appl Mater Interfaces 4:5727–5731
296. Xie KP, Wu Q, Wang YY, Guo WX, Wang MY, Sun L, Lin CJ (2011) Electrochem Commun 13:1469–1472
297. Xie KP, Sun L, Wang CL, Lai YK, Wang MY, Chen HB, Lin CJ (2010) Electrochim Acta 55:7211–7218
298. Mohapatra SK, Kondamudi N, Banerjee S, Misra M (2008) Langmuir 24:11276–11281
299. Zhang N, Liu S, Fu X, Xu YJ (2011) J Phys Chem C 115:9136–9145
300. Ye M, Gong J, Lai Y, Lin C, Lin Z (2012) J Am Chem Soc 134:15720–15723
301. Wang C, Yin L, Zhang L, Liu N, Lun N, Qi Y (2010) ACS Appl Mater Interfaces 2:3373–3377
302. Chen YC, Pu YC, Hsu YJ (2012) J Phys Chem C 116:2967–2975
303. Lai YK, Gong JJ, Lin CJ (2012) Int J Hydrogen Energy 37:6438–6446
304. Yu Y, Zhang MZ, Chen J, Zhao YD (2012) Dalton Trans 42:885–889
305. Bai H, Liu Z, Sun DD (2012) J Am Ceram Soc 96:942–949
306. Smitha VS, Baiju KV, Perumal P, Ghosh S, Warrier KG (2012) Eur J Inorg Chem 2012:226–233
307. K. M. Shrestha, C. M. Sorensen and K. J. Klabundea, J. Mater. Res., 1, 1-9
308. Lü X, Huang F, Wu J, Ding S, Xu F (2011) ACS Appl Mater Interfaces 3:566–572
309. Diamant Y, Chen S, Melamed O, Zaban A (2003) J Phys Chem B 107:1977–1981
310. Furukawa S, Shishido T, Teramura K, Tanaka T (2011) ACS Catalysis 2:175–179
311. Pan J, Hühne SM, Shen H, Xiao L, Born P, Mader W, Mathur S (2011) J Phys Chem C 115:17265–17269
312. Song KY, Park MK, Kwon YT, Lee HW, Chung WJ, Lee WI (2001) Chem Mater 13:2349–2355
313. Sun L, Bu JF, Guo WX, Wang YY, Wang MY, Lin CJ (2012) Electrochem Solid-State Lett 15:E1–E3
314. Katoh R, Furube A, Yoshihara T, Hara K, Fujihashi G, Takano S, Murata S, Arakawa H, Tachiya M (2004) J Phys Chem B 108:4818–4822
315. Jiang X, Zhang Y, Jiang J, Rong Y, Wang Y, Wu Y, Pan CX (2012) J Phys Chem C 116:22619–22624
316. Naldoni A, Allieta M, Santangelo S, Marelli M, Fabbri F, Cappelli S, Bianchi CL, Psaro R, Dal V (2012) Santo. J Am Chem Soc 134:7600–7603
317. Tominaka S, Tsujimoto Y, Matsushita Y, Yamaura K (2011) Angew Chem Int Ed 50:7418–7421
318. Zuo F, Bozhilov K, Dillon RJ, Wang L, Smith P, Zhao X, Bardeen C, Feng P (2012) Angew Chem Int Ed 124:6327–6330
319. Gu D, Lu Y, Yang B (2008) Chem Commun 2453–2455
320. Sayed FN, Jayakumar O, Sasikala R, Kadam R, Bharadwaj SR, Kienle L, Schürmann U, Kaps S, Adelung R, Mittal J (2012) J Phys Chem C 116:12462–12467

321. Kitano M, Funatsu K, Matsuoka M, Ueshima M, Anpo M (2006) J Phys Chem B 110:25266–25272
322. Gu DE, Yang BC, Hu YD (2008) Catal Commun 9:1472–1476
323. Wang CL, Wang MY, Xie KP, Wu Q, Sun L, Lin ZQ, Lin CJ (2011) Nanotechnology 22:305607
324. Sato S (1986) Chem Phys Lett 123:126–128
325. Sato S, Nakamura R, Abe S (2005) Appl Catal A 284:131–137
326. Lai YK, Huang JY, Zhang HF, Subramaniam VP, Tang YX, Gong DG, Sundar L, Sun L, Chen Z, Lin CJ (2010) J Hazard Mater 184:855–863
327. Cao J, Zhang Y, Tong H, Li P, Kako T, Ye J (2012) Chem Commun 48:8649–8651
328. Bacsa R, Kiwi J, Ohno T, Albers P, Nadtochenko V (2005) J Phys Chem B 109:5994–6003
329. Li Y, Ma G, Peng S, Lu G, Li S (2008) Appl Surf Sci 254:6831–6836
330. Chen D, Jiang Z, Geng J, Wang Q, Yang D (2007) Ind Eng Chem Res 46:2741–2746
331. Chen X, Burda C (2008) J Am Chem Soc 130:5018–5019
332. Dong F, Wang H, Wu Z (2009) J Phys Chem C 113:16717–16723
333. Sun H, Liu H, Ma J, Wang X, Wang B, Han L (2008) J Hazard Mater 156:552–559
334. Wu G, Wang J, Thomas DF, Chen A (2008) Langmuir 24:3503–3509
335. Dong F, Guo S, Wang H, Li X, Wu Z (2011) J Phys Chem C 115:13285–13292
336. Wei F, Ni L, Cui P (2008) J Hazard Mater 156:135–140
337. In S, Orlov A, Berg R, García F, Pedrosa-Jimenez S, Tikhov MS, Wright DS, Lambert RM (2007) J Am Chem Soc 129:13790–13791
338. Zong X, Xing Z, Yu H, Chen Z, Tang F, Zou J, Lu GQ, Wang L (2011) Chem Commun 47:11742–11744
339. Li L, Shi J, Li G, Yuan Y, Li Y, Zhao W (2013) New J Chem 37:451–457
340. Santos RS, Faria GA, Giles C, Leite CAP, Barbosa HS, Arruda MAZ, Longo C (2012) ACS Appl Mater Interfaces 4:5555–5561
341. Liu X, Geng D, Wang X, Ma S, Wang H, Li D, Li B, Liu W, Zhang Z (2010) Chem Commun 46:6956–6958
342. Cao G, Li Y, Zhang Q, Wang H (2010) J Am Ceram Soc 93:1252–1255
343. Zhang J, Pan C, Fang P, Wei J, Xiong R (2010) ACS Appl Mater Interfaces 2:1173–1176
344. Dai G, Yu J, Liu G (2011) J Phys Chem C 115:7339–7346
345. Wang Y, Zhang Y, Zhao G, Tian H, Shi H, Zhou T (2012) ACS Appl Mater Interfaces 4:3965–3972
346. Vogel R, Hoyer P, Weller H (1994) J Phys Chem 98:3183–3188
347. Kim W, Tachikawa T, Majima T, Choi W (2009) J Phys Chem C 113:10603–10609
348. D. Zhang, G. Li, X. Yang and C. Y. Jimmy, *Chem. Commun.,* 2009, **0**, 4381-4383
349. Peng L, Xie T, Lu Y, Fan H, Wang D (2010) Phys Chem Chem Phys 12:8033–8041
350. Wang C, Shao C, Zhang X, Liu Y (2009) Inorg Chem 48:7261–7268
351. Anderson C, Bard AJ (1997) J Phys Chem B 101:2611–2616
352. William L IV, Kostedt I, Ismail AA, Mazyck DW (2008) Ind Eng Chem Res 47:1483–1487
353. Fu X, Clark LA, Yang Q, Anderson MA (1996) Environ Sci Technol 30:647–653
354. Ding S, Yin X, Lü X, Wang Y, Huang F, Wan D (2011) ACS Appl Mater Interfaces 4:306–311
355. Shao Z, Zhu W, Li Z, Yang Q, Wang G (2012) J Phys Chem C 116:2438–2442
356. Kang Q, Liu S, Yang L, Cai Q, Grimes CA (2011) ACS Appl Mater Interfaces 3:746–749
357. Liu B, Wang D, Zhang Y, Fan H, Lin Y, Jiang T, Xie T (2012) Dalton Trans 42:2232–2237
358. Wang S, Zhang X, Zhou G, Wang ZS (2012) Phys Chem Chem Phys 14:816–822
359. Kim JY, Kang SH, Kim HS, Sung YE (2009) Langmuir 26:2864–2870
360. Yu H, Xue B, Liu P, Qiu J, Wen W, Zhang S, Zhao H (2012) ACS Appl Mater Interfaces 4:1289–1294
361. Jung HS, Lee JK, Nastasi M, Lee SW, Kim JY, Park JS, Hong KS, Shin H (2005) Langmuir 21:10332–10335
362. Shinde DV, Mane RS, Oh IH, Lee JK, Han SH (2012) Dalton Trans 41:10161–10163

363. Pang S, Xie T, Zhang Y, Wei X, Yang M, Wang D, Du Z (2007) J Phys Chem C 111:18417–18422
364. Cao T, Li Y, Wang C, Zhang Z, Zhang M, Shao C, Liu Y (2011) J Mater Chem 21:6922–6927
365. Li X, Hou Y, Zhao Q, Chen G (2011) Langmuir 27:3113–3120
366. Muduli S, Lee W, Dhas V, Mujawar S, Dubey M, Vijayamohanan K, Han SH, Ogale S (2009) ACS Appl Mater Interfaces 1:2030–2035
367. Liu B, Huang Y, Wen Y, Du L, Zeng W, Shi Y, Zhang F, Zhu G, Xu X, Wang Y (2012) J Mater Chem 22:7484–7491
368. Kim H, Moon G, Monllor-Satoca D, Park Y, Choi W (2011) J Phys Chem C 116:1535–1543
369. Zhang H, Lv X, Li Y, Wang Y, Li J (2009) ACS Nano 4:380–386
370. Liu J, Bai H, Wang Y, Liu Z, Zhang X, Sun DD (2010) Adv Funct Mater 20:4175–4181
371. Hou C, Zhang Q, Li Y, Wang H (2012) J Hazard Mater 205:229–235
372. Wojtoniszak M, Zielinska B, Chen X, Kalenczuk RJ, Borowiak-Palen E (2012) J Mater Sci 47:3185–3190
373. Yang N, Zhang Y, Halpert JE, Zhai J, Wang D, Jiang L (2012) Small 11:1762–1770
374. Lee JS, You KH, Park CB (2012) Adv Mater 24:1084–1088
375. Cottineau T, Albrecht A, Janowska I, Macher N, Bégin D, Ledoux MJ, Pronkin S, Savinova E, Keller N, Keller V (2012) Chem Commun 48:1224–1226
376. Kim IY, Lee JM, Kim TW, Kim HN, Kim H, Choi W, Hwang SJ (2012) Small 7:1038–1048
377. Peining Z, Nair AS, Shengjie P, Shengyuan Y, Ramakrishna S (2012) ACS Appl Mater Interfaces 4:581–585
378. Zhang XY, Li HP, Cui XL, Lin Y (2010) J Mater Chem 20:2801–2806
379. Liu S, Liu C, Wang W, Cheng B, Yu J (2012) Nanoscale 4:3193–3200
380. Tu W, Zhou Y, Liu Q, Tian Z, Gao J, Chen X, Zhang H, Liu J, Zou Z (2012) Adv Funct Mater 22:1215–1221
381. Sun L, Zhao Z, Zhou Y, Liu L (2012) Nanoscale 4:613–620
382. Sher Shah MSA, Park AR, Zhang K, Park JH, Yoo PJ (2012) ACS Appl Mater Interfaces 4:3893–3901
383. Zhang X, Sun Y, Cui X, Jiang Z (2012) Int J Hydrogen Energy 37:811–815
384. Jiang B, Tian C, Pan Q, Jiang Z, Wang JQ, Yan W, Fu H (2011) J Phys Chem C 115:23718–23725
385. Libisch F, Stampfer C, Burgdörfer J (2009) Phys Rev B 79:115423
386. Ritter KA, Lyding JW (2009) Nat Mater 8:235–242
387. Ponomarenko L, Schedin F, Katsnelson M, Yang R, Hill E, Novoselov K, Geim A (2008) Science 320:356–358
388. Zhuo S, Shao M, Lee ST (2012) ACS Nano 6:1059–1064

http://www.springer.com/978-1-4471-6472-2

Low-cost Nanomaterials
Toward Greener and More Efficient Energy Applications
Lin, Z.; Wang, J. (Eds.)
2014, VI, 488 p. 287 illus., Hardcover
ISBN: 978-1-4471-6472-2